The timing of magmatism and subsequent alteration of basaltic rocks cored at the base of IODP Site U1513, Naturaliste Plateau, southwestern Australia

Lloyd T. White[1]*, Marnie A. Forster[2], Dominique Tanner[1], Maria Luisa G. Tejada[3], Richard Hobbs[4], IODP Expedition 369 Science Party[5]

1. GeoQuEST Research Centre, School of Earth, Atmospheric and Life Sciences, University of Wollongong, NSW, Australia
2. Research School of Earth Sciences, The Australian National University, ACT, Australia
3. Institute for Marine Geodynamics, Japan Agency for Marine-Earth Science and Technology, 2-15 Natsushima-cho, Yokosuka-shi, Kanagawa 237-0061, Japan
4. Department of Earth Sciences, University of Durham, Durham, DH1 3LE, United Kingdom
5. https://iodp.tamu.edu/scienceops/precruise/swaustralia/participants.html

*Corresponding author: Lloyd White (lloydw@uow.edu.au)

Abstract

An 82.2 m thick sequence of basaltic rocks was recovered from a deep-sea core on the eastern flank of the Naturaliste Plateau, offshore southwestern Australia during International Ocean Discovery Program (IODP) Expedition 369. The basaltic rocks were cored at the base of IODP Site U1513 and represent the acoustic basement of the Mentelle Basin. The recovered materials consist of subaerial to shallow-water basalt flows interbedded with volcaniclastic beds and cross-cutting dolerite dykes, all of which have been altered to some degree. Existing paleomagnetic data obtained from the overlying sedimentary sequences indicate that the basaltic sequence cored at Site U1513 was deposited before 130.9 Ma. Here we present the results of $^{40}Ar/^{39}Ar$ step-heating experiments conducted on whole-rock samples of two basalt flows and six dolerite dykes to provide greater certainty of the timing of magmatism. Each sample was characterised using optical and scanning electron microscopy together with x-ray fluorescence (XRF) and x-ray diffraction (XRD) analyses. The dolerite dykes are the only rocks to record the primary cooling age of the magmatic event (135.4 ± 4.0 Ma). This magmatism was contemporaneous with rifting that preceded the break-up of Greater India from Australia/Antarctica and is potentially associated with the Greater Kerguelen large igneous province. The basalt flows record younger ages (117.9–110.4 Ma) that make no sense when considering the available stratigraphic data from the overlying sequences. Instead, these younger ages most likely reflect a phase of hydrothermal alteration and resetting of the argon systematics. This is because the vesicular basalts are more porous than the dolerite dykes, meaning that hydrothermal fluids preferentially flowed through the basalt, not the dolerite. This interpretation was validated by examining structural features within the overlying sedimentary sequences, which showed that hydrothermal veins are only found in the basaltic sequence as well as the overlying Hauterivian– early Aptian volcaniclastic-rich sedimentary sequence. This indicates that hydrothermal alteration occurred after the deposition of the volcaniclastic sequence, most likely at 115.0 ± 1.7 Ma. A tectonic reconstruction that shows the distribution of magmatism associated with the Greater Kerguelen large igneous province indicates that the earliest

phases of magmatism occurred within an ellipse with a NW–SE oriented long-axis. The reconstruction also shows that the Naturaliste Plateau was some distance from known sources of magmatism, which suggests that the hydrothermal activity on the Naturaliste Plateau may have been driven by a local source of magmatism that remained active during the Aptian.

Keywords: Kerguelen; Mentelle; argon; geochronology; petrology; Gondwana; large igneous province

1. Introduction

The initial phase of break-up between what are now recognised as the Indian, Australian and Antarctic plates coincided with the extrusion of flood basalts near the margins of each plate (e.g. Storey 1995; Coffin et al., 2002; Ingle et al., 2002). These basaltic flows are exposed in south-eastern Tibet (Zhu et al., 2005; 2008; 2009; Liu et al., 2015), north-eastern India (Baksi et al., 1987; Baksi 1995; Sarkar et al., 1996; Kent et al., 2002; Coffin et al., 2002), and southwestern Australia (Frey et al., 1996; Coffin et al., 2002; Ingle et al., 2004; Olierook et al., 2015; 2016; 2019) (Figure 1). Other similar Cretaceous volcanic rocks have also been obtained from dredged material from the Naturaliste and Wallaby plateaux offshore southwestern Australia (Coleman et al., 1982; Direen et al., 2017; Olierook et al., 2015; 2017) as well as younger basaltic rocks (~120 to 110 Ma) that have been sampled from the present-day Kerguelen Plateau (Coffin et al., 2002; Duncan 2002). All of these mafic magmatic rocks are considered to be part of the Greater Kerguelen large igneous province (LIP) which was primarily active between 147–124 Ma (Olierook et al., 2017; 2019). The extent of basaltic magmatism associated with this LIP also likely encompasses the Bruce Rise, submerged crust offshore Enderby Land based on interpretations of geophysical data (Stagg et al., 2004; 2006; Golynsky et al., 2013).

Some consider that the Greater Kerguelen LIP magmatism was associated with hotspot activity centred beneath the Kerguelen Plateau. The details regarding the source of this plume differ between authors, with some proposing magmatism was driven by a single mantle plume source (e.g. Storey et al., 1992; Ingle et al., 2004; Zhu et al., 2008; 2009), others proposing a single-plume source that segregated into several 'diapirs' due to shear flow in the mantle (e.g. Coffin et al., 2002), or from several plumes sourcing different parent material (e.g. Coffin et al., 2002). Others have proposed that the >130 Ma phase of magmatism, such as the Bunbury Basalt in southwestern Australia might instead be explained by other mechanisms, such as decompression melting of a zone of subcontinental lithospheric mantle (e.g., Olierook et al., 2016; 2019). Regardless of what geodynamic mechanism is responsible for the Greater Kerguelen LIP, it is important that we develop a better understanding of the spatio-temporal distribution of the magmatic products – particularly considering the links between LIPs and their potential to impact the global climate at different stages through Earth's history. This paper therefore aims to provide new geochronological, petrological and geochemical data from variably altered basaltic rocks that were cored from the Naturaliste Plateau, offshore southwestern Australia which we hypothesise are part of the Greater Kerguelen LIP. These rocks were collected as part of Expedition 369 of the International Ocean Discovery Program (IODP) (Huber et al., 2019). The basaltic rocks were cored at IODP Site U1513 (Lat. 33º47.6196'S, Long. 112º29.1339'E) in two separate holes (U1513D and U1513E) that are laterally spaced by ~20m (Huber et al., 2019; Tejada et al., 2020) (Figure 1).

2. Regional setting of the Naturaliste Plateau and Mentelle Basin

The Naturaliste Plateau and Mentelle Basin are part of the Australian Plate and found immediately offshore the southwestern corner of mainland Australia (Figure 1). The Naturaliste Plateau is a regional topographic high, covering an area of ~90,000 km^2 (Borissova, 2002; Direen et al., 2017). It is separated from the southwest Australian mainland by a ~170 km-wide trough, which essentially demarcates the Mentelle Basin (Figure 1) (Borissova et al., 2010; Maloney et al., 2011).

Our knowledge of the geology and tectonic history of the Naturaliste Plateau and Mentelle Basin has been derived from several offshore dredging and coring campaigns (e.g., Hayes et al., 1975; Coleman et al., 1982; Halpin et al., 2008; Direen et al., 2017), as well as from interpretations of gravity, magnetic and seismic imagery (e.g. Borissova 2002; Borissova et al., 2010; Johnston et al., 2010; Maloney et al., 2011). Additional insights have been gained over time through detailed petrographic, geochemical and isotopic studies of recovered samples (e.g. Halpin et al., 2008; Direen et al., 2017; Huber et al., 2019; Lee et al., 2020; Wainman et al., 2020). For instance, zircon U-Pb ages obtained from gneiss samples dredged from the Naturaliste Plateau indicate that these rocks were metamorphosed during the Cambrian Pinjarra Orogeny of southwestern Australia (Halpin et al., 2008). These metamorphic rocks are interpreted to represent part of the rifted basement of the Naturaliste Plateau.

The region underwent several deformation phases. The initial phase of stretching of the Naturaliste Plateau and Mentelle Basin potentially occurred during the Late Carboniferous to Early Permian, followed by a phase of Mid-Permian to Early Jurassic thermal subsidence (Borissova et al., 2010). A second phase of extension occurred during the Middle Jurassic, creating a series of half-grabens (Borissova et al., 2010). Stretching continued during the Early Cretaceous, driven by the break-up of Greater India from the Australian/Antarctic plate (Direen et al., 2007; Borissova et al., 2010; Harry et al., submitted). Many consider that this break-up event is marked by a Valanginian to Hauterivian unconformity surface which is laterally continuous across much of the southwestern Australian margin (Direen et al., 2007; Borissova et al., 2010; Maloney et al., 2011). This interpretation has since been confirmed by palynological data obtained from IODP site U1515 (Huber et al., 2019; Figure 1), which sampled Jurassic to earliest Cretaceous fluvio-lacustrine sedimentary rocks beneath the unconformity on the continental slope of the eastern Mentelle Basin (Wainman et al., 2020). The unconformity surface developed prior to, or at the same time as a period of sub-aerial volcanism. The volcanics are defined by highly reflective horizons as well as several kilometre-scale mounded structures that are observed in seismic reflection imagery (e.g. Figure 2) (Borissova et al., 2010; Maloney et al., 2011). While Maloney et al., (2011) interpreted that these features might be volcanic or carbonate in origin, the cores obtained during IODP Expedition 369 found no evidence of carbonates and hence concluded that these were most likely volcanic rocks (Huber et al., 2019).

Interpretations of the available seismic reflection imagery from the region also showed that a series of east to northeast striking extensional faults occur within the central and southern Mentelle Basin (Borissova et al., 2010; Maloney et al., 2011). These faults offset the Valanginian–Hauterivian unconformity, as well as the overlying basaltic, Hauterivian–early Aptian volcaniclastic-rich and Albian sedimentary sequences (Figure 2). The seismic imagery interpreted using the stratigraphic control provided by Site U1513 cores indicate that the Mentelle Basin and Naturaliste Plateau underwent another phase of rifting during the Late Cretaceous (Figure 2). This phase of stretching was driven by broadly north-south to northwest-southeast directed crustal extension that has been attributed to the rifting that eventually led to the generation of oceanic crust at ~84 Ma between what are now recognised as the Australian and Antarctic plates (Sayers et al., 2001), followed by the eastward propagation of the developing plate boundary and the final separation of Australia and Antarctica at circa 45 Ma (e.g., White et al., 2013; van den Ende et al., 2017).

3. Igneous rocks obtained from the Mentelle Basin and Naturaliste Plateau

IODP Expedition 369 recovered the first in-situ basaltic material from the Mentelle Basin/Naturaliste Plateau at Site U1513 (Huber et al., 2019; Tejada et al., 2020) (Figures 1 and 3). The core material shows a good correlation between the lithologies recovered from Holes U1513D and U1513E (Figure 3). Combined, the two holes recovered an 82.2 m sequence of black to greenish grey basaltic flows with varying degrees of green, brown and red alteration overprint, interbedded with several volcaniclastic sedimentary horizons and cross-cut by dolerite dykes. The physical properties, petrology and preliminary geochemistry of the volcanic sequence were described in Huber et al., (2019) with detailed volcanic stratigraphy and additional petrographic and core descriptions reported by Tejada et al., (2020). These earlier works classified the volcanic sequence within Site U1513 as 'Lithostratigraphic Unit VI'. This sequence was further subdivided into nine lithologic units based on the stratigraphy and observable differences in lithology, texture and alteration (Huber et al., 2019; Tejada et al., 2020). Their stratigraphic position is shown in Figure 3 and a summary of the characteristics of these nine sub-units are provided in Table 3 of Tejada et al., (2020).

Biostratigraphic and palaeomagnetic data obtained during Expedition 369 (Huber et al., 2019) indicate that the basaltic rocks cored at Site U1513 must be older than the base of magnetic chron M10Nn.1n (134.5 Ma) according to the geomagnetic time scale of Ogg (2012) (Figure 3). However, more recent studies of Early Cretaceous magnetic chrons that use isotopic age data intercalibrated with astrochronology indicate that the base of chron M10Nn.1n (and the top of the basaltic sequence of interest to this study) may be as young as ~130.9 Ma (see Lee et al., 2020 and Harry et al., submitted for calculations and further discussion). The basaltic rocks must also be younger than the Jurassic to earliest Cretaceous (Berriasian) fluvio-deltaic sediments dated beneath the regional unconformity (Wainman et al., 2020). These data indicate that the basaltic rocks erupted between ~145.0 Ma and ~130.9 Ma.

Here we attempt to provide clarity about the age of the basaltic units recovered from IODP Site U1513, particularly their age with respect to other basaltic sequences identified in southwestern Australia and the Greater Kerguelen LIP. We also attempt to determine the age of possible alteration of the basaltic rocks and to consider potential regional events that may explain the timing of alteration.

4. Samples and Methodology

Three basaltic flows and five cross-cutting dolerite dykes were examined in this study. Quartered sections of working half core sections from Holes U1513D and U1513E were sampled during IODP Expedition 369 to further characterise their petrography, geochemistry and age. Care was taken to examine the core visually and sample the least altered sections. The sample details are summarised in Table 1, with further metadata including International Geo Sample Numbers (IGSN) are provided in Supplementary Data 1. The stratigraphic context of the eight samples that were dated in this study is shown in Figure 3. Core photographs of each sample are provided in Figure 4.

The samples are 4 cm to 15 cm quarter core lengths divided into polished thin sections and whole-rock powders for geochemical and mineralogical characterisation using petrographic analysis, x-ray diffraction (XRD) and scanning electron microscopy (SEM). The sub-sample dated using $^{40}Ar/^{39}Ar$ mass spectrometry was collected immediately above or below whole-rock x-ray fluorescence (XRF) and XRD samples (Table 1; Supplementary Data 1).

The eight sections of the core that were selected for XRF, XRD and $^{40}Ar/^{39}Ar$ measurements were cut into smaller segments with a trim saw, before being washed, dried in an oven for 24 h at 60°C and then pulverised in a tungsten-carbide ring mill for 60 s. An aliquot of the powdered material was ground further by hand within an agate mortar and pestle and was set aside for XRD analyses.

Please insert Table 1.

4.1 Petrography

Polished thin sections were examined using a standard petrographic microscope. Additional observations were made at higher magnification using the PhenomXL benchtop scanning electron microscope with an energy dispersive spectrometer housed at the University of Wollongong.

4.2 X-ray Diffraction

The powdered sample material was further examined using a Malvern PanAnalytical Empyrean Series 3 x-ray diffractometer at the Research School of Earth Sciences at the Australian National University. This instrument is equipped with a Bragg-Brentano$_{HD}$ divergent beam optic and a PIXcel$_{3D}$ detector (1D scanning mode, 3.347 degrees active length) using CoKα radiation. The samples were spiked with 20 wt.% corundum (Baikalox, 1 μm), suspended on a low-background holder (Si or quartz) and analysed over a range of 4-85° 2θ, with a step width of 0.0131303° 2θ and a total dwell time of 71 s per step. Phase identification was carried out with the software Match! and the Crystallographic Open Database (Inorganic, Revision 211633 25.10.2018). Phase quantification was performed using the FullProf plugin within Match! and used the 20 wt.% corundum spike as a reference value to quantify the wt.% of other mineral phases. The spectra and mineral phase calculations are reported in Supplementary File 2.

4.3 Whole-rock geochemistry

The whole-rock major and trace element composition of each sample was determined using a Spectro Ametek XEPOS III energy dispersive XRF spectrometer at the University of Wollongong. Major element data were obtained from the analysis of glass-fusion beads. Trace element data were measured using pressed powder pellets. Several geological reference materials were run as unknowns alongside the basaltic samples to ensure the results were accurate (Supplementary File 3). The major element data were reduced using the volatile content obtained from a loss-on-ignition (LOI) measurement of each sample. However, we report the results on a volatile-free basis. The iron concentration for each sample is reported as total Fe_2O_3.

4.4 Argon–Argon Dating

The eight samples selected for argon dating were crushed and separated in the Australian National University Mineral Separation Laboratory. The most pristine sections of samples were selected before being crushed and sieved, with the 250–420 µm size fraction being retained for argon dating. Aggregates were de-slimed, dried and later washed in deionised water. The air-dried material was then hand-picked and wrapped in aluminium packets. These were placed into a quartz irradiation canister together with aliquots of the flux monitor GA1550. Packets containing K_2SO_4 and CaF_2 were placed in the middle of the canister to monitor ^{40}Ar production from potassium. The samples were then sent for irradiation at the UC Davis MNRC nuclear reactor in California, USA prior to analysis. Irradiated samples were unwrapped on their return to ANU, weighed and rewrapped in tin-foil ready for analysis in the mass spectrometer. Samples were dropped into the furnace causing the tin-foil to melt and the gas was pumped away prior to analysis of sample. Backgrounds were measured prior to each step analysis and subtracted from each step analysis. The basaltic samples were analysed with 29 steps and with temperatures of the overall schedule rising from 450°C to 1450°C (Lovera et al., 1989). The furnace was degassed at 1450°C for 20 min. This was repeated 4 times and gas was pumped away prior to each analysis. Temperature steps in the schedule were increased in small increments to minimize mixing of different gas populations on each step (Supplementary File 4).

Flux monitors, GA 1550, were analysed using a CO_2 continuous wave laser and the ARGUS VI Mass Spectrometer. Gas released from each step was exposed to three different Zr-Al getters to remove active gases for 10 min, the purified gas then being isotopically analysed in the mass spectrometer. The furnace was decontaminated between samples. Corrections for argon produced by interaction of neutrons with K and Ca were made using the following correction factors: $(^{36}Ar/^{37}Ar)_{Ca}$: 2.297E-04, $(^{39}Ar/^{37}Ar)_{Ca}$: 7.614E-04, $(^{40}Ar/^{39}Ar)_{K}$: 5.992E-02, $(^{38}Ar/^{39}Ar)_{K}$: 1.158E-02 and $(^{38}Ar)_{Cl}/(^{39}Ar)_{K}$: 8.170E-02 (Tetley et al., 1980). ^{40}K abundances and decay constants are taken from standard values recommended by the IUGS subcommission on Geochronology (Steiger and Jager, 1977). Stated precisions for $^{40}Ar/^{39}Ar$ ages include all uncertainties in the measurement of isotope ratios and are quoted at the one sigma level (Supplementary File 4).

The reported data were corrected for system backgrounds, mass discrimination, fluence gradients and atmospheric contamination. Errors associated with the age determinations are one sigma uncertainties and exclude errors in the age of the fluence monitor GA1550 (Supplementary File 4). The $^{40}Ar/^{39}Ar$ dating technique is described in detail by MacDougall and Harrison (1999). Readers are directed to Supplementary File 5 for additional information on the argon dating methodology.

4.5 Structural Analysis

High-resolution core photos obtained from IODP Site U1513 were examined to assist our interpretation of the argon apparent age spectra and the geological evolution of the region. In doing so, we documented which lithostratigraphic units above the basaltic sequence had been cross-cut by faults and veins. We considered the age of these sequences using the biostratigraphic data reported in Huber et al., (2019) to establish the timing of alteration and/or thermal perturbations that might influence the apparent age spectra obtained from argon measurements.

5. Results

5.1 Petrography and mineralogy

5.1.1 IODP Sample: U1513D-66R-3, 93-105 – Basaltic Flow

Sample U1513D-66R-3, 93-105 is from a basaltic flow that was cored at 694 m below sea floor (mbsf); near the top of the Volcanic Unit 3 (Figures 2, 3 and 4a). This rock is moderately altered and contains three populations of phenocrysts: (1) 10 modal% rounded to sub-rounded plagioclase phenocrysts and glomerocrysts; (2) 3 modal% tabular feldspar phenocrysts, and (3) pseudomorphic replacement of equant to slightly elongate hexagonal prismatic crystals (likely pseudomorphed after clinopyroxene) that amount to ~1 modal%. The rounded to sub-rounded plagioclase phenocrysts and glomerocrysts are typically 8 mm in length, some contain growth zones rich in small melt inclusions. Plagioclase in some of the rounded glomerocrysts is fractured along grain boundaries, with fracturing occurring before or during emplacement. The tabular feldspar crystals are generally 1.5 mm in length, with no evidence of abrasion or rounding. The hexagonal prismatic pseudomorphs are typically 2 mm in length, replaced by fine-grained secondary minerals including chlorite, calcite and Fe-oxide. No evidence of the primary hexagonal prismatic mineral is preserved, although this texture was seen replacing clinopyroxene in other samples examined during this study. The groundmass comprises 40 modal% felty plagioclase microlites, generally 100 µm in length within a pervasively altered matrix. Anastomosing chlorite and serpentine veinlets infill fractures in the matrix as well as both feldspar populations.

The XRD analysis of this sample indicates that 73% of the material is either amorphous and/or composed of minerals that are <5 µm in size (i.e., below the grain-size detection limit of the XRD). The remainder consists of labradorite (18%), augite (3%), serpentine (3%) and other unidentified phases (3%) (Figure 5).

5.1.2 IODP Sample: U1513D-67R-2, 58-73 – Dolerite dyke

Sample U1513D-67R-2, 58-73 is a plagioclase-phyric dolerite that intrudes a basaltic flow (equivalent to the sample discussed above) at 696 mbsf (Figure 3). Sample U1513D-67R-2, 58-73 is altered, contains plagioclase phenocrysts, plagioclase-augite glomerocrysts, large rounded augite and plagioclase crystals as well as fine-grained minerals (Figure 4b). In thin section, we observed an ~2 cm xenolith with a high proportion of interstitial green glass. In the remainder of the sample, three populations of phenocrysts were identified: (1) 3 modal% rounded, 6 mm long, fractured and partially replaced plagioclase crystals; (2) 1 modal% glomerocrysts of fractured and partially replaced feldspar laths with equant to slightly elongate prismatic augite crystals (up to 4 mm in length) and; (3) 1 modal% pervasively altered sub-rounded 6 mm long augite crystals. The groundmass comprises felty plagioclase microlites around 75 µm in length, in a pervasively altered matrix. The remainder of the groundmass exhibits a patchy texture, defined by fine-grained alteration minerals.

The XRD analysis of this sample indicates that 53% of the material is either amorphous and/or material that is <5 µm in size. The remainder of the sample consists of labradorite (15%), augite (18%), serpentine (6%), vermiculite/clay (5%) and other unidentified phases (3%) (Figure 5).

5.1.3 IODP Sample U1513D-69R-4, 76-95 – Basaltic Flow

Sample U1513D-69R-4, 76-95 is from an older basaltic flow (Unit 7) at 714.22 mbsf (Figure 3). It is a plagioclase-phyric basalt that is highly altered with a vuggy, porphyritic texture (Figure 4c). Plagioclase and augite phenocrysts are only partially preserved. Highly altered sub-rounded plagioclase phenocrysts and pseudomorphs after plagioclase phenocrysts are up to 3 mm in length. More than 50 area % of the remaining plagioclase phenocrysts are replaced by anastomosing veinlets filled with fine-grained secondary minerals, although some crystals are completely replaced by fine-grained secondary minerals. The groundmass is almost completely altered by fine-grained minerals, although 250 µm plagioclase microlites are occasionally preserved. Both ~4 mm vugs and interstices in the groundmass contain zoned, syntaxial, cavity-fill textures.

XRD analyses indicate that 81% of this sample consists of either amorphous material and/or material that is <5 µm in size. The remainder consists of labradorite (7%), protoanthophyllite (3%), serpentine (2%), vermiculite/clay (1%) and other unidentified phases (6%) (Figure 5).

5.1.4 IODP Sample U1513D-70R-4, 11-26 – Dolerite dyke

Sample U1513D-70R-4, 11-26 is a plagioclase-phyric dolerite that intrudes a basaltic flow (equivalent to the sample discussed in Section 5.1.3) at 723 mbsf (Figure 3). The sample is slightly altered, with plagioclase glomerocrysts in a plagioclase–clinopyroxene groundmass (Figure 4d). The glomerocrysts are 1–7 mm in length, sub-angular and contain fractured, oscillatory-zoned plagioclase crystals. The glomerocrysts constitute 2 modal% of the thin section. The groundmass comprises 50 modal% felty plagioclase microlites ~200 µm in length, 30 modal% clinopyroxene ~100 µm in length, 5 modal% opaque minerals ~30 µm in length and some fine-grained secondary minerals.

XRD analyses indicate that 54% of the sample consists of either amorphous material and/or material that is <5 µm in size. The remainder consists of labradorite (16.5%), diopside (23.5%), ganophyllite (2%) and other unidentified phases (4%) (Figure 5).

5.1.5 IODP Sample U1513D-71R-2, 110-124 – Basalt Flow

Sample U1513D-71R-2, 110-124 is a plagioclase-phyric basaltic flow (Unit 7) cored at 725 mbsf (Figure 2). The sample is moderately altered, with mineralised vesicles and distinct plagioclase glomerocrysts containing sieve-textured cores (Figure 4e). The vesicles are spherical, 0.5–2.5 mm in diameter and filled with fine-grained secondary minerals. The glomerocrysts constitute 8 modal% of the sample. They are 0.8–7 mm in length and sub-rounded; oscillatory zonation is present in most crystals. Glomerocryst rims are mostly intact with minor fractures. However, nearly all glomerocryst cores are highly altered, preserving relict sieve textures, replaced with fine-grained secondary alteration minerals. Rare, highly-altered clinopyroxene phenocrysts constitute <1 modal% of the sample. The groundmass is highly altered, with partial preservation of felty plagioclase microlites ~250 μm in length and rare relict fragments of altered clinopyroxene. The remainder of the groundmass is composed of fine-grained secondary alteration minerals.

XRD analyses indicate that 70% of the sample either consists of amorphous material and/or material that is <5 μm in size. The remainder consists of labradorite (11%), diopside (6%), ganophyllite (7.5%), and other unidentified phases (5.5%) (Figure 5).

5.1.6 IODP Sample U1513D-73R-4, 62-78 – Dolerite dyke

Sample U1513D-73R-4, 62-78 is a plagioclase-phyric dolerite that intrudes a basaltic flow (Unit 7) at 742 mbsf (Figure 3). The sample is moderately altered, contains sparse tabular plagioclase phenocrysts, pseudomorphs after a hexagonal prismatic mineral (presumably clinopyroxene), a singular plagioclase glomerocryst, all in an altered groundmass with vesicles filled with secondary minerals (Figure 4f). Tabular plagioclase phenocrysts are ~1 mm in length and constitute <1 modal% of the thin section. The plagioclase phenocrysts are relatively unaltered, with only minor fractures. Most display oscillatory zonation. One ~5 mm glomerocryst was observed, containing fractured, oscillatory-zoned, angular plagioclase laths up to 4 mm in length. The glomerocryst also contains ~2 mm equant prismatic crystals replaced by fine-grained minerals, likely psuedomorphed after clinopyroxene. These altered, equant prismatic crystals are also present as phenocrysts within the groundmass. Spherical to sub-spherical vesicles are 0.25–1 mm in length, filled with fine-grained secondary minerals. The groundmass consists of 40 modal% felty plagioclase microlites ~250 μm in length, ~15% interstitial clinopyroxene and the remainder of the groundmass is replaced by fine-grained secondary minerals.

XRD analyses indicate that 56% of the sample consists of either amorphous material and/or material that is <5 µm in size. The remainder consists of labradorite (19%), diopside (20%) and other unidentified phases (5%) (Figure 5).

5.1.7 IODP Sample U1513D-74R-1, 120-132 – Dolerite dyke

Sample U1513D-74R-1, 120-132 is a plagioclase-phyric dolerite that intrudes a basaltic flow (Unit 7) at 744 mbsf (Figure 3). The sample is slightly altered, with angular, blocky plagioclase glomerocrysts within a plagioclase-clinopyroxene groundmass (Figure 4g). Glomerocrysts are 3–7 mm in length, and constitute 8 modal% of the thin section. Only blocky, angular plagioclase crystals with oscillatory zonation and occasional sieve textures were observed in glomerocrysts. The plagioclase is fractured, but relatively unaltered. Plagioclase microlites (~250 µm) constitute 40% of the groundmass and define a weak trachytic texture. The remainder of the groundmass comprises interstitial clinopyroxene, opaque minerals and fine-grained secondary minerals.

XRD analyses indicate that 64% of the sample consists of either amorphous material and/or material that is <5 µm in size. The remainder consists of labradorite (15%), diopside (17%) and other unidentified phases (4%) (Figure 5).

5.1.8 IODP Sample U1513E-8R-4, 118-119 – Dolerite dyke

Sample U1513E-8R-4, 118-119 is a plagioclase-phyric dolerite that was sampled at 760 mbsf (Unit 9) (Figure 4h). It cross-cuts the deepest volcanic unit sampled at IODP Site U1513 (Figure 3). This sample was selected because it represents the least altered material near the base of drill-core U1513E.

The thin section of this sample contains pervasively altered plagioclase phenocrysts and one intact clinopyroxene phenocryst in a highly altered groundmass. Elongate, sub-angular plagioclase phenocrysts are ~750 µm in length and are almost completely altered. They constitute <0.05 modal% of the sample. The sub-rounded clinopyroxene phenocryst is ~2 mm in length and fractured along cleavage planes. The groundmass is moderately altered. Felty ~150 µm plagioclase microlites constitute ~30% of the groundmass. The remainder of the groundmass exhibits a patchy texture, defined by fine-grained alteration minerals.

XRD analyses indicate that 72% of the sample consists of either amorphous material and/or material that is <5 µm in size. The remainder consists of andesine (16%), clinopyroxene (8%), vermiculite/clay (1%) and other unidentified phases (3%) (Figure 5).

5.2 Geochemistry

Loss-on-ignition measurements for the analysed samples shows that these rocks have variable volatile contents, with values ranging between 4.2% to 17.3% (Table 2). The bulk-rock major element data indicate that each of the samples are classified geochemically as basalt (e.g., when using a total-alkali vs. silica plot). However, we expect that the major element data will not necessarily reflect the primary composition of the basaltic rocks. This is because all of the samples have relatively high-volatile contents and because our analysis of thin sections shows that all of the samples record evidence of post-crystallisation alteration. However, immobile element (Ti, Nb, Y and Zr) concentrations indicate that all of the analysed samples plot within the 'basalt' field when using the classifications proposed by Pearce (1996) (Table 2; Figure 6). It is worth noting that all Cu values for the samples selected for dating are relatively low (30 – 100 ppm) despite other sections of the basaltic sequence showing native copper and malachite growth within veins (Table 2). It is also worth noting that the dolerite dyke intersected at 760 mbsf (Sample U1513E-8R-4, 118-119) yielded very high Cl concentrations (17,330 ppm – i.e., 1.7 wt%), which we took into consideration when interpreting the argon mass spectrometry data for this sample (see Section 5.3).

5.3 Argon Geochronology

The results of the step heating experiments conducted on the analysed samples are shown in Figure 7a to 7h, Table 3 and Supplementary File 4. Two of the basaltic flows that were dated yield similar results. Sample U1513D-66R-3, 93-105 yielded an apparent age of 115.8 +/- 2.1 Ma (Figure 7a), while Sample U1513D-69R-4, 76-95 yielded an apparent age of 113.4 +/- 3.0 Ma (Figure 7c). The step heating experiment for the other basalt flow (Sample U1513D-71R-2, 110-124) failed to produce a clear plateau (Figure 7e). We interpreted this spectrum to indicate this sample had a maximum possible age of 129.5 +/- 1.0 and a minimum possible age of 104.8 +/- 1.3 Ma (Figure 7e).

The majority of the dolerite samples obtained apparent ages between 129.5 Ma and 148.4 Ma (Figure 7b, 7d, 7f, 7g; Table 3). These ages are all within analytical uncertainty of one another (Table 3).

One other dolerite dyke (Sample U1513E-8R-4, 118-119) yielded an age of 182.1 +/- 5.2 Ma. However, this age was calculated from a plateau defined by three steps (Figure 7h; Table 3). An analysis of the percentage of gas released during the step heating experiment for this sample indicates that this sample likely had considerable excess argon contamination causing large errors in the apparent age, particularly at the beginning and the end of the experiment (Figure 7f). These errors correlate with an increase in the chlorine/potassium gas ratio as measured by the mass spectrometer (Supplementary File 4), which is supported further by high Cl concentrations identified during the XRF analysis of this sample (Table 2; Supplementary File 3). Considering that the apparent age determined by this sample is influenced by chlorine and potentially excess argon, we expect that the apparent age determined for this sample is not geologically significant.

5.4 Structural Analysis

Our analysis of the timing of when sedimentary sequences that overlie the basaltic rocks were cross-cut by faults and/or veins is presented in Table 4 and summarised in Figure 8.

The cross-cutting relations, together with biostratigraphic and palaeomagnetic data indicate that two (or more) phases of faulting occurred after the deposition of the basaltic flows. The earliest episode is characterised by calcite veins that are only evident within the early Aptian to Hauterivian volcaniclastic-rich sandstone sequence (Unit V) as well as calcite veins and serpentinised fault planes in the underlying basaltic flows (Unit VI) (Figure 3 and 8). These structures must have therefore developed between 125 Ma (the youngest age proposed for Unit V: Lee et al., 2020) and before the initial deposition of unaltered Albian–Cenomanian claystones (Unit IV) at ~110 Ma (Huber et al., 2019) (Table 4).

The younger episode of deformation consists of small-scale fault planes that offset the Albian to Campanian sedimentary sequences that overlie the Hauterivian–early Aptian volcaniclastic-rich sandstone unit (Figure 8a-c). These non-mineralised fault planes most likely developed between 93.7 Ma and the present day. They may simply be a series of small-scale faults that developed after deposition and partial lithification of the sedimentary units that they cross-cut. The slip direction cannot be determined from direct observation of the core, yet we assume that these younger faults are extensional based on the dominant structures observed in the regional seismic imagery (e.g. Figure 2). These faults might represent evidence of polygonal faulting in the basin that was discussed by Maloney et al., (2011).

6. Discussion

All of the samples that were dated in this study show evidence of secondary mineral growth and volatile contents that are higher than would be expected from a pristine, unaltered sample (Table 2). The mineralogy, geochemistry and available stratigraphic control must therefore be considered when interpreting the apparent age determined for each sample (Figure 7).

There is a clear correlation between the primary mineral content (feldspar and clinopyroxene) and volatile content of each sample (Figure 9a). That is, samples that have a higher proportion of primary minerals, have lower volatile contents and *vice versa*. This relationship is also apparent when considering the volatile content and primary mineral contents with the apparent age determined by argon dating (Figure 9b and 9c respectively). For instance, the basaltic flows (Samples: U1513D-66R-3, 93-105; U1513D-69R-4, 76-95; U1513D-71R-2, 110-124) have higher LOI values, lower primary mineral contents and younger apparent ages relative to those samples that record ages of 149–130 Ma, all of which are dolerite dykes with higher primary mineral contents and lower volatile contents (Figure 9b-c). Considering these data, we interpret the 149–130 Ma apparent ages as being representative of the crystallisation age of the dolerite dykes. This is because these ages do not contradict the biostratigraphic and paleomagnetic age control (Figure 2) and because these samples retain more primary minerals than the other samples examined as part of this study. A weighted mean age of 135.4 ± 4.0 Ma (MSWD = 0.36) was calculated by combining the apparent ages determined for Samples U1513D-67R-2, 58-73, U1513D-70R-4, 11-26, U1513D-73R-4, 62-78 and U1513D-74R-1, 120-132. We take this weighted mean age as being representative of the timing of the dolerite dyke emplacement at IODP Site U1513. This age also serves as a minimum age for the extrusive basalts that were cored at Site U1513.

The apparent ages (115–113 Ma) determined for two of the basaltic flows (Samples U1513D-66R-3, 93-105 and U1513D-69R-4, 76-95) are younger than the overlying sedimentary rocks (Figure 3). This means that the apparent ages determined for these samples cannot represent when these basalts were emplaced, and instead likely reflect resetting of the argon systematics due to hydrothermal alteration. This assertion seems reasonable considering that the rocks have been altered, as demonstrated by our petrographic, XRD and LOI measurements. This is further supported by our structural analysis of the core, which demonstrated that calcite vein networks are present in the

Hauterivian to Albian sedimentary rocks that overlie the basaltic sequence, but not in younger sequences. Considering the uncertainties associated with the calculated ages, we propose that the Mentelle Basin experienced an episode of hydrothermal alteration between 117.9 Ma and 110.4 Ma. A weighted mean age of these two results yields a value of 115.0 ± 1.7 Ma (MSWD = 0.43, p(x2) = 0.51). The 130.5 Ma to 103.5 Ma apparent age range determined for Sample U1513D-71R-2, 110-124 also potentially reflects partial resetting of the argon systematics because of this period of hydrothermal activity.

We assume that the dolerite dykes and sills represent the intrusive equivalents of the basaltic flows, where earlier basalt flows were cross-cut by younger dolerite that fed younger extrusive flows, only to be cross-cut by younger dolerite intrusions and overlain by younger basalt flows. This continued thermal activity might explain why Sample U1513E-8R-4, 118-119, the deepest sample to be dated in this study had considerable contamination and yielded an implausible geological age (Figure 7h; Table 3). However, the apparent ages determined for the basalts and dolerites is somewhat odd, in that these seemingly contemporaneously emplaced rocks record different ages. We explain these different ages as being a function of the porosity differences between the basalts and dolerites (Figure 9d). Shipboard measurements of moisture and density that were conducted during Expedition 369 were used to calculate the porosity for discrete 1 cm_3 samples of rock extracted from the core (Huber et al., 2019). These data show that the basalts have porosities of 24.8% to 47.7% (with a median value of 43.5%) (Figure 9d). On the other hand, the dolerites have porosities between 10.3% and 17.9% (with a median value of 16.0%) (Figure 9d). This difference is most likely due to the vesicular nature of the basalts (even though the porosity values were determined from samples where most vesicles had been infilled with secondary minerals). Since the basalts (as well as the interbedded volcaniclastic sequences that were cored in Hole U1513D: Figure 9d) are more porous than the dolerites, we expect that hydrothermal fluids would preferentially flow through the basalt and volcaniclastic rocks, with the hot fluids resetting the argon systematics, as well as depositing secondary minerals and altering primary minerals.

6.1 Generation of flood basalts during India-Australia-Antarctica break-up

The basaltic rocks that were cored at IODP Site U1513 were emplaced at 135.4 ± 4.0 Ma. This indicates that these rocks are broadly coincident with the 135.7 Ma to 125.9 Ma ages reported for samples of basalt, dolerite, rhyolite, granophyre and monzodiorite collected during dredging campaigns around the edge of the Naturaliste Plateau (Direen et al., 2017), as well as the recently refined ages proposed for the Bunbury Basalt of SW Australia (136.96 ± 0.43 Ma; 132.71 ± 0.43 Ma; 130.45 ± 0.82 Ma: Olierook et al., 2016)[1]. The basaltic rocks that were cored at Site U1513 were therefore most-likely to have been generated due to the same mechanism(s) that were responsible for the 147–124 Ma Greater Kerguelen LIP (Olierook et al., 2017; 2019). During this time, the crust between the Indian, Australian and Antarctic plates was being thinned to the point where new ocean crust was developed between India and Australia/Antarctica (e.g. Gibbons et al., 2012; Williams et al., 2013; Ali and Aitchison 2014).

The spatio-temporal relationship between the timing and location of magmatism associated with the Greater Kerguelen LIP is best understood by reconstructing the position of the various tectonic plates and microcontinental fragments together with the position of dated rock samples. We used PaleoGIS together with the plate boundaries and Euler poles that were presented in van den Ende et al., (2017) to create reconstructions at 5 million-year intervals between 145 Ma and 110 Ma (Figures 10 and 11). These images show the spatio-temporal context of the samples that were dated in this study together with the best geochronological data available for the Greater Kerguelen LIP (Olierook et al., 2017; 2019)

[1] Readers should note that the ages we report for the Bunbury Basalt are those provided by Olierook et al. (2016), who reviewed the veracity of earlier reported ages (e.g., by Frey et al., 1996; Coffin et al., 2002) and provided updated age values for the Bunbury Basalt.

using a mantle reference frame. The reconstructions demonstrate that magmatism was active as Greater India rifted and drifted away from Australia/Antarctica (Figures 10 and 11). The reconstructions also show that during the earlier stage of break-up, magmatism was located near the edges of the dissecting plates, essentially along continental transform faults that developed to accommodate plate divergence (Figures 10b-d and 11a-b). This perhaps explains why there is an apparent NW–SE trend to the 140–125 Ma magmatism (Figures 10b–d and 11a) – although we also recognise that this might be due to a sampling bias.

Magmatism associated with Greater Kerguelen LIP continued on the Kerguelen Plateau as well as the Indian and Antarctic plates during the Aptian and Albian (Coffin et al., 2002; Duncan 2002) (Figure 11). The Naturaliste Plateau was approximately 500 km from the Kerguelen Plateau during these times and there is no other evidence for a primary source of magmatism on the Naturaliste Plateau during the Aptian and Albian (Figure 11). We anticipate that hydrothermal activity responsible for the 115.0 ± 1.7 Ma alteration of the Early Cretaceous basaltic and volcaniclastic sequences cored at Site U1513 was associated with the continuation of magmatism on the Naturaliste Plateau or surrounding region during the Aptian–Albian – potentially at depth.

7 Conclusions

An 82.2 m-thick sequence of basaltic flows, interbedded with volcaniclastic sedimentary sequences and cross-cut by dolerite dykes was recovered from the eastern flank of the Naturaliste Plateau at IODP Site U1513. Eight samples of what were considered the least altered examples of basalt and dolerite from this sequence were dated using argon mass spectrometry to improve our understanding of the stratigraphy and tectonic history of the Naturaliste Plateau and the Mentelle Basin. The dating campaign shows that basaltic magmatism occurred at 135.4 ± 4.0 Ma – indicating that the magmatism was coincident with the Greater Kerguelen LIP and the break-up of Greater India from Australia/Antarctica. The argon results also record evidence of a subsequent phase of hydrothermal alteration at

115.0 ± 1.7 Ma. This period of alteration was most likely driven by hot fluids associated with magmatism and hydrothermal activity beneath the Naturaliste Plateau that continued into the Aptian–Albian.

Acknowledgements

The authors thank the Captain and Crew of *D/V JOIDES Resolution* and the technical staff of the International Ocean Discovery Program (IODP) for the successful implementation of Expedition 369. All shipboard data are publicly available at http://web.iodp.tamu.edu/LORE/. All analytical work presented here was funded by a post-cruise analytical funding grant provided by the Australian and New Zealand IODP Consortium (ANZIC) to L.W. The samples that were analysed as part of this study have also been registered with International Geological Sample Numbers (IGSNs) using the System for Earth Sample Registration (SESAR), available at: geosamples.org/. ANZIC is thanked for allowing L.W. to participate in Expedition 369. ANZIC was supported by the Australian Government through the Australian Research Council's LIEF funding scheme (LE160100067). We thank Ulrike Troitzsch (ANU), Davood Vasegh (ANU), Shane Paxton (ANU) and Jose Abrantes (UOW) for sample preparation and analytical support. L.W. thanks the Rothwell Group for supplying an academic licence for PaleoGIS which was used to create the plate reconstruction models in this paper.

References

Ali, J.R., Aitchison, J.C., 2014. Greater India's northern margin prior to its collision with Asia. Basin Research 26, 73–84. doi:10.1111/bre.12040

Baksi, A.K., Barman, T.R., Paul, D.K., Farrar, E., 1987. Widespread Early Cretaceous flood basalt volcanism in eastern India: geochemical data from the Rajmahal-Bengal-Sylhet traps. Chemical Geology 63, 133-141

Baksi, A.K., 1995. Petrogenesis and timing of volcanism in the Rajmahal flood basalt province, northeastern India. Chemical Geology 121, 73-90.

Borissova, I., 2002. Geological framework of the Naturaliste Plateau, Record 2002/20. Geoscience Australia, Canberra, 44 p.

Borissova, I., Bradshaw, B., Nicholson, C., Struckmeyer, H.I.M., Payne, D., 2010. New exploration opportunities on the southwest Australian margin—deep-water frontier Mentelle Basin. APPEA Journal, 50th Anniversary Issue, 47–60.

Coffin, M.F., Pringle, M.S., Duncan, R.A., 2002. Kerguelen hotspot magma output since 130 Ma. Journal of Petrology, 43, 1121-1139.

Coleman, P.J., Michael, P.J., Mutter, J.C., 1982. The origin of the Naturaliste Plateau, SE Indian Ocean: Implications from dredged basalts. Journal of the Geological Society of Australia 29, 457–468. doi:10.1080/00167618208729228

Direen, N.G., Borissova, I., Stagg, H.M.J., Colwell, J.B., Symonds, P.A., 2007. Nature of the continent–ocean transition zone along the southern Australian continental margin: a comparison of the Naturaliste Plateau, SW Australia, and the central Great Australian Bight sectors. In: Karner, G.D., Manatschal, G., Pinheiro, L.M. (Eds.), Imaging, Mapping and Modelling Continental Lithosphere Extension and Breakup. Geological Society, London, pp. 235–261.

Direen, N.G., Cohen, B.E., Maas, R., Frey, F.A., Whittaker, J.M., Coffin, M.F., Meffre, S., Halpin, J.A., Crawford, A.J., 2017. Naturaliste Plateau: constraints on the timing and evolution of the Kerguelen Large Igneous Province and its role in Gondwana breakup. Australian Journal of Earth Sciences 64, 851–869. doi:10.1080/08120099.2017.1367326

Duncan, R.A., 2002. A time frame for construction of the Kerguelen Plateau and Broken Ridge. Journal of Petrology 43, 1109–1119.

Frey, F.A., Mcnaughton, N.J., Nelson, D.R., 1996. Petrogenesis of the Bunbury Basalt, Western Australia: interaction between the Kerguelen plume and Gondwana lithosphere? Earth and Planetary Science Letters 144, 163-183.

Gibbons, A.D., Barckhausen, U., van den Bogaard, P., Hoernle, K., Werner, R., Whittaker, J.M., Müller, D. 2013. Constraining the Jurassic extent of Greater India: Tectonic evolution of the West Australian margin. Geochemistry, Geophysics, Geosystems 13, Q05W13, doi:10.1029/2011GC003919, 25 p.

Golynsky, A.V., Ivanov, S.V., Kazankov, A.J., Jokat, W., Masolov, V.N., Frese, von, R.R.B., and the ADMAP Working Group. 2013. New continental margin magnetic anomalies of East Antarctica. Tectonophysics 585, 172–184. doi:10.1016/j.tecto.2012.06.043

Halpin, J.A., Crawford, A.J., Direen, N.G., Coffin, M.F., Forbes, C.J., Borissova, I., 2008. Naturaliste Plateau, offshore Western Australia: A submarine window into Gondwana assembly and breakup. Geology 36, 807-810. doi:10.1130/G25059A.1

Harry, D.L., Tejada, M.L.G., Lee, E.Y., Wolfgring, E., Wainman, C.C., Brumsack, H.-J., Schnetger, B., Kimura, J.-I., Riquier, L., Borissova, I., Hobbs, R., Jiang, T., Li, Y-X., Maritati, A., Martinez, M., Richter, C., Tagliaro, G.T., White, L.T., the IODP Expedition 369 Shipboard Science Party. Submitted. Evolution of the Southwest Australian Rifted Continental Margin During Breakup of East Gondwana: Results from IODP Expedition 369. Geochemistry, Geophysics, Geosystems.

Hayes, D. E., Frakes, L. A., Barrett, P. J. 1975. Initial Reports of the Deep Sea Drilling Project, Leg 28. Deep Sea Drilling Program, College Station, TX.

Huber, B.T., Hobbs, R.W., Bogus, K.A., Batenburg, S.J., Brumsack, H.-J., do Monte Guerra, R., Edgar, K.M., Edvardsen, T., Harry, D.L., Hasegawa, T., Haynes, S.J., Jiang, T., Jones, M.M., Kuroda, J., Lee, E.Y., Li, Y.-X., MacLeod, K.G., Maritati, A., Martinez, M., O'Connor, L.K., Petrizzo, M.R., Quan, T.M., Richter, C., Riquier, L., Tagliaro, G.T., Tejada, M.L.G., Wainman, C.C., Watkins, D.K., White, L.T., Wolfgring, E., Xu, Z., 2019. Site U1513. In: Hobbs, R.W., Huber, B.T., Bogus, K.A., Expedition 369 Scientists (Eds.), Australia Cretaceous Climate and Tectonics. Proceedings of the International Ocean Discovery Pro- gram. IODP, College Station, TX.

Ingle, S., Weis, D., Frey, F.A., 2002. Indian continental crust recovered from Elan Bank, Kerguelen plateau (ODP Leg 183, site 1137). Journal of Petrology 43, 1241-1257.

Ingle, S., Scoates, J.S., Weis, D., Brügmann, G., Kent, R.W., 2004. Origin of Cretaceous continental tholeiites in southwestern Australia and eastern India: insights from Hf and Os isotopes. Chemical Geology 209, 83–106. doi:10.1016/j.chemgeo.2004.04.023

Johnston, S., Hackney, R., Nicholson, C. 2010. Distribution of igneous facies and potential-field modelling of the Mentelle Basin, southwestern margin, Australia. ASEG Extended Abstracts, 1-4. https://doi.org/10.1081/22020586.2010.12041965

Kent, R.W., Pringle, M.S., Müller, R.D., Saunders, A.D., Ghose, N.C., 2002. ^{40}Ar/^{39}Ar geochronology of the Rajmahal basalts, India, and their relationship to the Kerguelen Plateau. Journal of Petrology 43, 1141-1153.

Lee, E.Y., Wolfgring, E., Tejada, M.L.G., Harry, D.L., Wainman, C.C., Chun, S.S., Schnetger, B., Brumsack, H.-J., Maritati, A., Martinez, M., Richter, C., Li, Y.-X., Riquier, L., MacLeod, K.G., Waller, T.R., Borissova, I., Petrizzo, M.R., Huber, B.T., Kim, Y., Expedition 369 Science Party, 2020. Early Cretaceous subsidence of the Naturaliste Plateau defined by a new record of volcaniclastic-rich sequence at IODP Site U1513. Gondwana Research 82, 1–11. doi:10.1016/j.gr.2019.12.007

Liu, Z., Zhou, Q., Lai, Y., Qing, C., Li, Y., Wu, J., Xia, X., 2015. Petrogenesis of the Early Cretaceous Laguila bimodal intrusive rocks from the Tethyan Himalaya: Implications for the break-up of Eastern Gondwana. Lithos 236-237, 190–202. doi:10.1016/j.lithos.2015.09.006

Lovera, O. M., F. M. Richter, & T. M. Harrison. 1989. ^{40}Ar/^{39}Ar thermochronometry for slowly cooled samples having a distribution of diffusion domain sizes. *Journal Geophysical Research,* **94**, 17, 917– 17,935.

McDougall, I., & T. M. Harrison (Eds.). 1999. Geochronology and Thermochronology by the ^{40}Ar/^{39}Ar Method, 2nd ed., 269 pp. Oxford Univ. Press, New York.

Maloney, D., Sargent, C., Direen, N.G., Hobbs, R.W., Gröcke, D.R., 2011. Re-evaluation of the Mentelle Basin, a polyphase rifted margin basin, offshore southwest Australia: new insights from integrated regional seismic datasets. Solid Earth 2, 107–123. doi:10.5194/se-2-107-2011

Ogg, J.G., 2012. Geomagnetic polarity timescale. In: Gradstein, F., Ogg, J.G., Schmitz, M., Ogg, G. (Eds.), The Geologic Time Scale. Elsevier, Amsterdam, pp. 85–113.

Olierook, H.K.H., Merle, R.E., Jourdan, F., Sircombe, K., Fraser, G., Timms, N.E., Nelson, G., Dadd, K.A., Kellerson, L., Borissova, I., 2015. Age and geochemistry of magmatism on the oceanic Wallaby Plateau and implications for the opening of the Indian Ocean. Geology 43, 971–974. doi:10.1130/G37044.1

Olierook, H.K.H., Jourdan, F., Merle, R.E., Timms, N.E., Kusznir, N., Muhling, J.R., 2016. Bunbury Basalt: Gondwana breakup products or earliest vestiges of the Kerguelen mantle plume? Earth and Planetary Science Letters 440, 20–32. doi:10.1016/j.epsl.2016.02.008

Olierook, H.K.H., Merle, R.E., Jourdan, F., 2017. Toward a Greater Kerguelen large igneous province: evolving mantle source contributions in and around the Indian Ocean. Lithos 282–283, 163–172.

Olierook, H.K.H., Jiang, Q., Jourdan, F., Chiaradia, M., 2019. Greater Kerguelen large igneous province reveals no role for Kerguelen mantle plume in the continental breakup of eastern Gondwana. Earth and Planetary Science Letters 511, 244–255. doi:10.1016/j.epsl.2019.01.037

Pearce, J. A., 1996. A User's Guide to Basalt Discrimination Diagrams, in Wyman, D. A., ed. Trace Element Geochemistry of Volcanic Rocks: Applications for Massive Sulphide Exploration: Geological Association of Canada, Short Course Notes, v. 12. P. 79-113.

Sarkar, A., Datta, A.K., Poddar, B.C., Bhattacharyya, B.K., Kollapuri, V.K., Sanwal, S., 1996. Geochronological studies of Mesozoic igneous rocks from eastern India. Journal of Southeast Asian Earth Sciences 13, 77–81.

Sayers, J., Symonds, P., Direen, N., Bernardel, G., 2001. Nature of the continent-ocean transition on the non-volcanic rifted margin of the central Great Australian Bight. Geological Society London Special Publications 187, 51–76.

Stagg, H. M. J., Colwell, J. B., Borissova, I., Ishihara, T., & Bernardel, G. 2006. The Bruce Rise Area, East Antarctica: Formation of a Continental Margin near the Greater India–Australia–Antarctica Triple Junction. Terra Antarctica, 13, 3–22.

Stagg, H. M. J., Colwell, J. B., Direen, N. G., O'Brien, P. E., Bernardel, G., Borissova, I., ... Ishihara, T. 2004. Geology of the continental margin of Enderby and Mac. Robertson Lands, East Antarctica: Insights from a regional data set. Marine Geophysical Research, 25, 183– 219.

Steiger, R. H., & E. Jager. 1977. Subcommission on geochronology: Convention on the use of decay constants in geo- and cosmochronology. *Earth Planetary Science Letters*, **36**, 359–362.

Storey, B.C., 1995. The role of mantle plumes in continental breakup: case histories from Gondwanaland. Nature 377, 301–308.

Tejada, M.L.G., Lee, E.Y., Chun, S.S., Harry, D.L., Riquier, L., Wainman, C.C., 2020. Data report: Petrology and volcanic stratigraphy at Site U1513, IODP Expedition 369. Proceedings of the International Ocean Discovery Program, 369. IODP, College Station, TX.

Tetley, N., I. McDougall, & H. R. Heydegger. 1980. Thermal neutron interferences in the $^{40}Ar/^{39}Ar$ dating technique. *Journal Geophysical Research*, **85**, 7201– 7205.

van den Ende, C., White, L.T., van Welzen, P.C., 2017. The existence and break-up of the Antarctic land bridge as indicated by both amphi-Pacific distributions and tectonics. Gondwana Research 44, 219–227. doi:10.1016/j.gr.2016.12.006

Wainman, C.C., Borissova, I., Harry, D.L., Hobbs, R.W., Mantle, D.J., Maritati, A., Lee, E.Y., Expedition 369 Scientists, 2020. Evidence for non-marine Jurassic to earliest Cretaceous sediments in the pre-breakup section of the Mentelle Basin, southwestern Australia. Aust J Earth Sci 67, 89-105. doi:10.1080/08120099.2019.1627581

White, L.T., Gibson, G.M., Lister, G.S., 2013. A reassessment of paleogeographic reconstructions of eastern Gondwana: Bringing geology back into the equation. Gondwana Research 24, 984–998. doi:10.1016/j.gr.2013.06.009

Whiteway, T., 2009. Australian Bathymetry and Topography Grid, June 2009. Record 2009/021. Geoscience Australia, Canberra. http://dx.doi.org/10.4225/25/53D99B6581B9A

Williams, S.E., Whittaker, J.M., Granot, R., Muller, D.R., 2013. Early India-Australia spreading history revealed by newly detected Mesozoic magnetic anomalies in the Perth Abyssal Plain. Journal of Geophysical Research: Solid Earth 118, 1–10, doi:10.1002/jgrb.50239

Zhu, D., et al. 2005. SHRIMP U-Pb zircon dating for the dacite of the Sangxiu Formation in the central segment of Tethyan Himalaya and its implications. Chinese Sci Bull 50, 563–6. doi:10.1360/04wd0281

Zhu, D., Mo, X., Pan, G., Zhao, Z., Dong, G., Shi, Y., Liao, Z., Wang, L., Zhou, C., 2008. Petrogenesis of the earliest Early Cretaceous mafic rocks from the Cona area of the eastern Tethyan Himalaya in south Tibet: Interaction between the incubating Kerguelen plume and the eastern Greater India lithosphere? Lithos 100, 147–173. doi:10.1016/j.lithos.2007.06.024

Zhu, D.C., Chung, S.L., Mo, X.X., Zhao, Z.D., Niu, Y., Song, B., 2009. The 132 Ma Comei-Bunbury large igneous province: Remnants identified in present-day southeastern Tibet and southwestern Australia. Geology 37, 583–586. doi:10.1130/G30001A.1

Table Captions

Table 1: An overview of the details of each sample examined in this study, including the sample number, depth and metadata about the core number and section. Details about the Stratigraphic Unit have been summarised from information provided in Tejada et al., (2020).

Table 2. Major (wt %) and Trace (µg/g) element composition of samples from Holes U1513D and U1513E as determined by XRF. Loss-on-ignition (LOI) data are also included.

Table 3. Summary of calculated ages determined from $^{40}Ar/^{39}Ar$ argon geochronological data.

Table 4. Biostratigraphic and palaeomagnetic age control from Huber et al., (2019) from samples that were examined above and below sedimentary sequences that are cross-cut by faults and veins within the material recovered from IODP Site U1513.

Figure Captions

Figure 1. Regional map of the Naturaliste Plateau and Mentelle Basin (yellow polygon), showing the dated Bunbury Basalt localities, Deep Sea Drilling Program (DSDP) Site 264 and IODP Sites cored during Expedition 369 (U1513, U1514, U1515 and U1516). The rocks that were recovered at the base of Site U1513 are the focus of this study. The location of the seismic line SWM07 that is shown in Figure 2 is displayed here. Bathymetric data were obtained from the Australian Bathymetry and Topography Grid (Whiteway, 2009).

Figure 2. Seismic line SWM07 shows the stratigraphy of the Mentelle Basin, supported by observations of the cored material recovered at IODP Site U1513. The strong reflector at the base of the sequence represents the top of the basaltic sequence (Unit VI) that is the focus of this study. These volcanic rocks are overlain by a Hauterivian–early Aptian volcaniclastic-rich sandstone (Unit V), Albian–Cenomanian claystone (Unit IV), Cenomanian claystone (Unit III), Cenomanian–Campanian ooze, chalk and silicified limestone (Unit II) and Late Miocene to Pleistocene ooze (Unit I). The seismic imagery shows that Units V and VI are faulted, with minor faults or reactivation of earlier faults also cross-cutting younger sequences. Please see Figure 1 for the location and orientation of the seismic line.

Figure 3. (a) Overview of the stratigraphy of IODP Site U1513 after Huber et al., (2019), based on observations of Hole U1513D, (b) palaeomagnetic data from the superconducting cryogenic rock magnetometer on the JOIDES Resolution (grey dots and lines) as well as from discrete samples (blue squares) after Huber et al., (2019). These data have been interpreted to suggest that the basaltic sequence (Unit VI) is older than M10Nn.1n, yet there is uncertainty about the assigned age as the contact between Unit V and Unit VI is unconformable, as well as because of uncertainties associated with which geomagnetic timescale is used. The numerical ages shown here correspond with those proposed by Lee et al., (2020) and Harry et al., (submitted). (c) Detailed interpretation of Unit VI, where 9 units

of basaltic flows, volcaniclastic beds and cross-cutting dolerite dykes were interpreted (after Tejada et al., 2020). The stratigraphic position of the samples examined in this study are also shown.

Figure 4. High-resolution core photographs that show the colour and texture of each of the samples that were examined in this study (Huber et al., 2019). The photographs are of the archive-half section of the U1513 core and are the equivalent of the material examined in this study. The position and amount of examined material is marked with a red dashed line.

Figure 5. Results of quantitative XRD analyses showing the modal mineralogy of each sample (arranged by depth). All of the samples show high amounts of amorphous material and secondary minerals, but relatively low percentages of primary minerals (plagioclase and clinopyroxene).

Figure 6. Geochemical data for each sample were determined by XRF and were plotted following the Zr/Ti vs. Nb/Y discriminator plot of Pearce (1996). This indicates that the basaltic flows and dolerite dykes are geochemically defined as 'basalt'.

Figure 7. Apparent age vs. the percentage of ^{39}Ar released were plotted following the argon step-heating experiments. Each sample was measured with 28 to 29 steps so as to eliminate mixing and allow potential plateau ages to consist of many steps (a to h). A weighted mean age was determined for each sample using either a plateau, a limit or asymptotes. In these samples the plateau ages are considered more robust age estimates e.g. plot a, b, c, f, g. Most of the samples show some evidence of excess argon in the initial steps and the final steps (e.g. plot h); (h) Sample U1513E-8R-4, 118-119 contained high chlorine concentrations (as determined by XRF), this resulted in high uncertainty and a geologically meaningless age.

Figure 8. Representative photographs of deformed sections of the U1513 core. (a-c) The upper units (Unit II, III and IV; for unit designations, please see Figure 3) are cross-cut by faults in places, leading to the juxtaposition of different sedimentary layers, potentially due to gravity/loading and soft-sediment deformation. The available biostratigraphic control (Huber et al., 2019) indicates that these structures are younger than 103.1 Ma. (d-j) More pervasive veining and fault brecciation only occurs in Unit V and VI (although we only show evidence from Unit V here). The available biostratigraphic control (Huber et al., 2019; Table 4) indicates that these structures all developed between 110 Ma and 130.9 Ma, but most likely between 110 Ma (the oldest available dates for Unit IV: Huber et al., 2019) and 125 Ma (the youngest available dates for Unit V: Lee et al., 2020).

Figure 9. (a) There is a correlation between increasing volatile content (as determined by loss-on-ignition) and decreasing primary mineral content of the basaltic samples that were examined in this study. (b) Samples that yielded the highest volatile contents yielded lower apparent ages compare to those samples with volatile contents of <6%. (c) Samples that yielded lower percentages of primary minerals yielded younger apparent ages compared to samples with higher primary mineral contents. (d) Shipboard moisture and density measurements were conducted on discrete samples of basalt, dolerite and volcaniclastic beds from Unit VI during Expedition 369 and were used to estimate the porosity of each sample (Huber et al., 2019) – these results show that basalt and volcaniclastic rocks have higher porosities compared to the dolerite dykes, which may mean that hydrothermal fluids preferentially flowed through basaltic flows and not the dolerite dykes, leading to younger apparent ages in the basaltic flows compared to the dolerite dykes which cross-cut them.

Figure 10. The position of the tectonic plates and microcontinental fragments were plotted at 5 Ma increments from (a) 145 Ma to (d) 130 Ma, following the Euler poles and plate boundaries used by van den Ende et al., (2017). The age and position of magmatic events were obtained from the revised compilation of reliable age data for the Greater Kerguelen

large igneous province provided by Olierook et al., (2019), together with the ages obtained in this study. The ‘appearance’ of the magmatic events factors in the uncertainty associated with each age.

Figure 11. The position of the tectonic plates and microcontinental fragments were plotted at 5 Ma increments from (a) 125 Ma to (d) 110 Ma, following the Euler poles and plate boundaries used by van den Ende et al., (2017). The age and position of magmatic events were obtained from the revised compilation of reliable age data for the Greater Kerguelen large igneous province provided by Olierook et al., (2019), together with the ages obtained in this study. The ‘appearance’ of the magmatic events factors in the uncertainty associated with each age.

Supplementary File Captions

Supplementary File 1: Metadata for each of the samples examined during this study.

Supplementary File 2: XRD results and calculations for the samples examined during this study.

Supplementary File 3: XRF results for the samples that were examined within this study as well as the results of reference materials that were run alongside the unknowns.

Supplementary File 4: Results of $^{40}Ar/^{39}Ar$ measurements obtained for each sample examined during this study

Supplementary File 5: Further details of the $^{40}Ar/^{39}Ar$ methodology, correction factors and sample preparation procedures.

Figure 1:

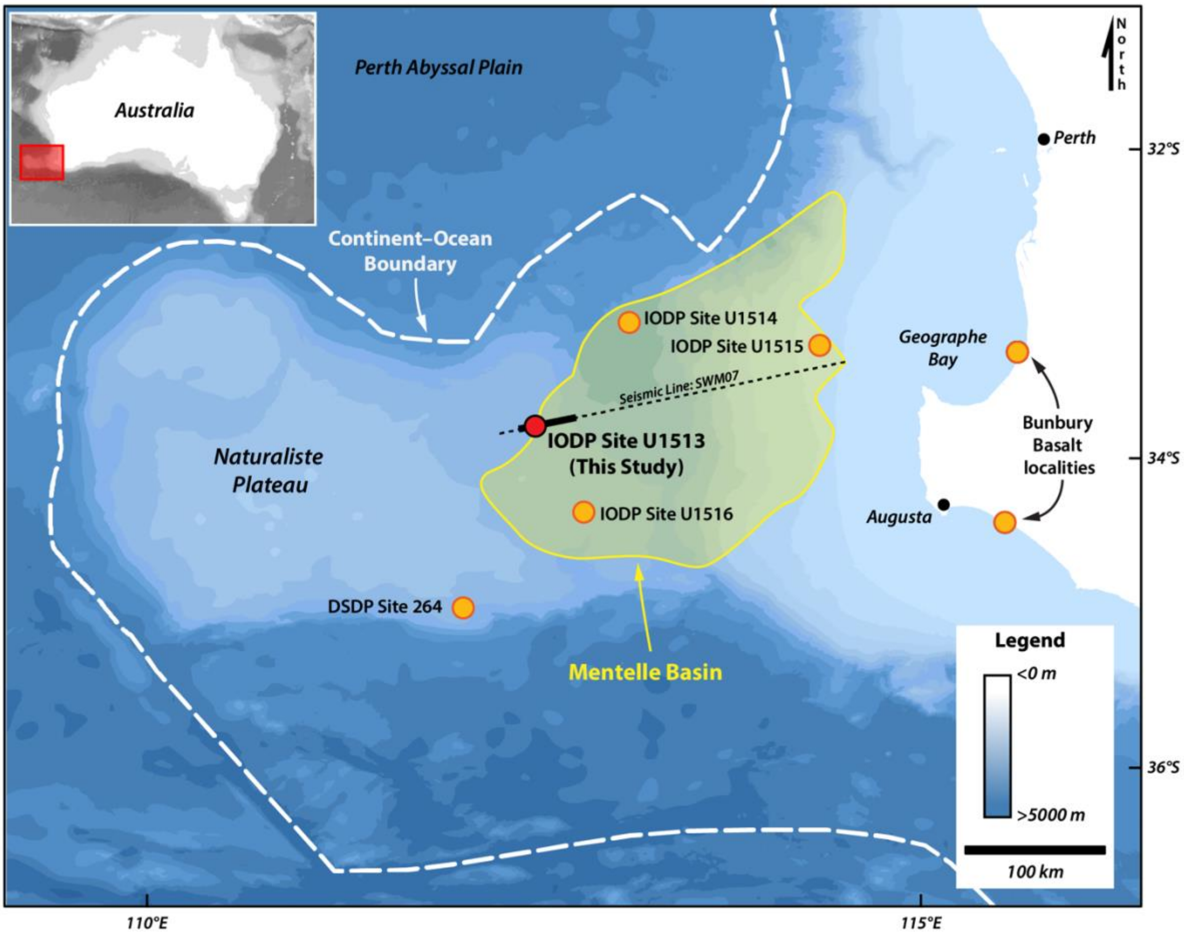

Australia
Perth Abyssal Plain
North
Perth
32°S
Continent–Ocean Boundary
IODP Site U1514
IODP Site U1515
Geographe Bay
Seismic Line: SWM07
IODP Site U1513 (This Study)
34°S
Naturaliste Plateau
Bunbury Basalt localities
Augusta
IODP Site U1516
DSDP Site 264
Mentelle Basin
Legend
<0 m
>5000 m
100 km
36°S
110°E
115°E

Figure 2:

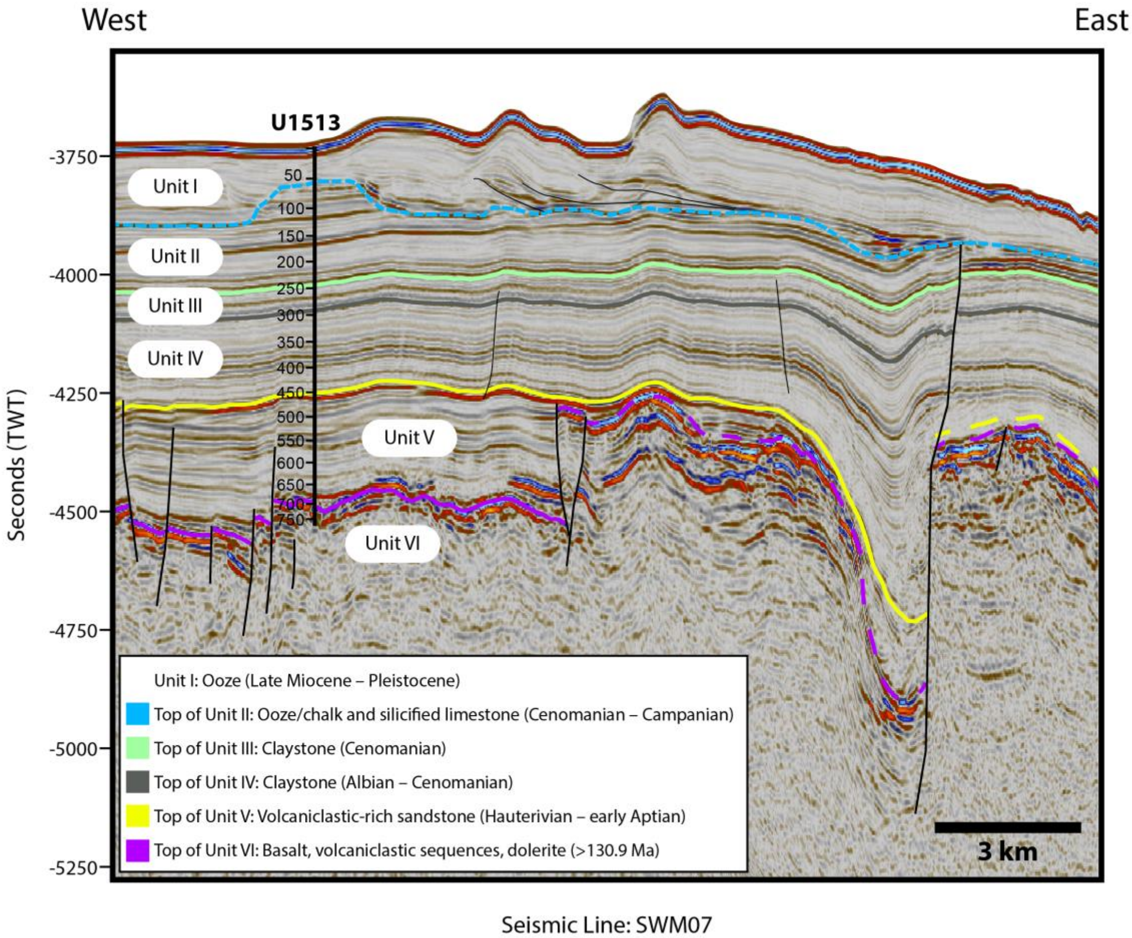
West
East
U1513
Unit I
Unit II
Unit III
Unit IV
Unit V
Unit VI
Seconds (TWT)
-3750
-4000
-4250
-4500
-4750
-5000
-5250
50
100
150
200
250
300
350
400
450
500
550
600
650
700
750
Unit I: Ooze (Late Miocene – Pleistocene)
Top of Unit II: Ooze/chalk and silicified limestone (Cenomanian – Campanian)
Top of Unit III: Claystone (Cenomanian)
Top of Unit IV: Claystone (Albian – Cenomanian)
Top of Unit V: Volcaniclastic-rich sandstone (Hauterivian – early Aptian)
Top of Unit VI: Basalt, volcaniclastic sequences, dolerite (>130.9 Ma)
3 km
Seismic Line: SWM07

Figure 3:

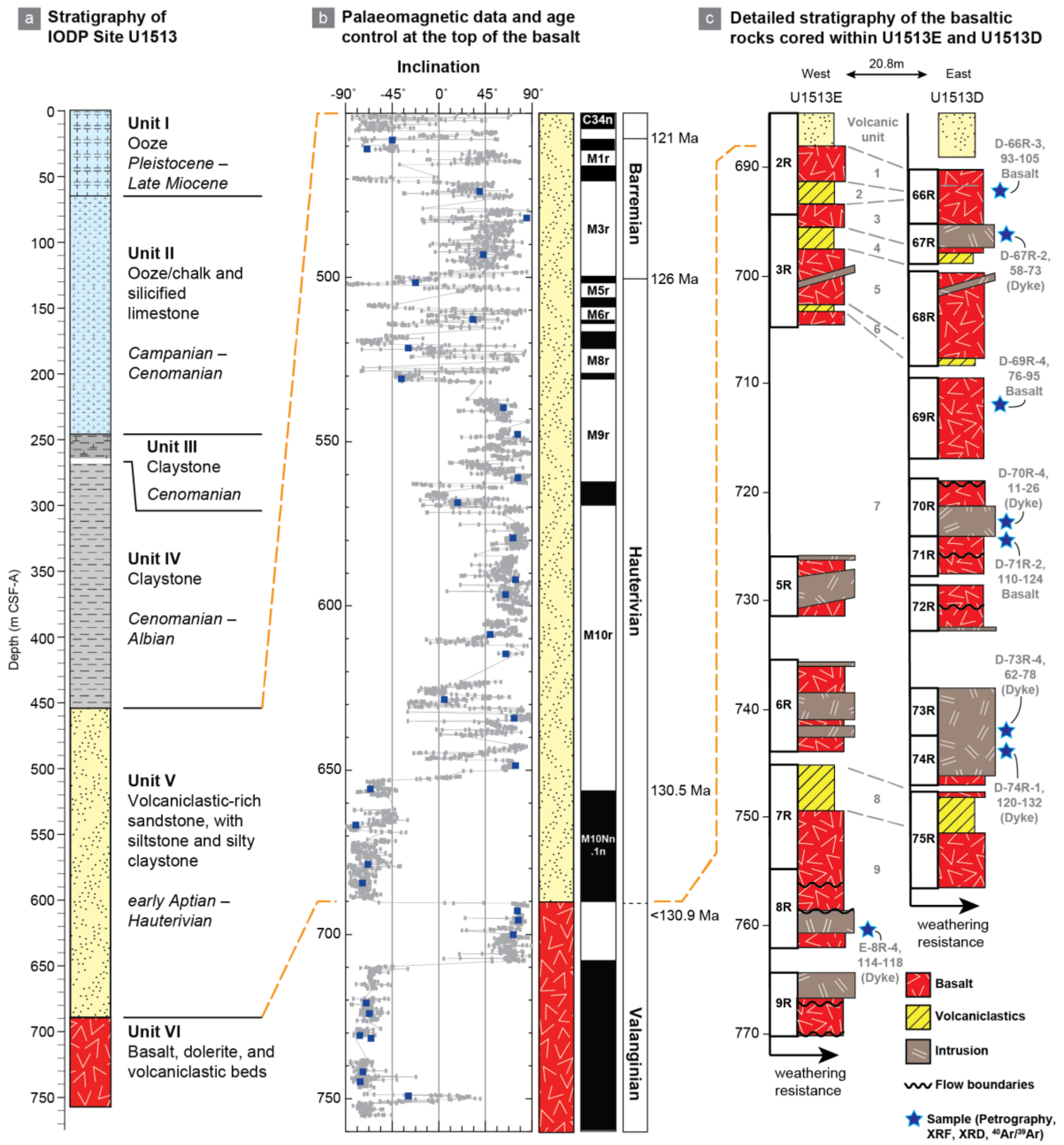

a Stratigraphy of IODP Site U1513
b Palaeomagnetic data and age control at the top of the basalt
c Detailed stratigraphy of the basaltic rocks cored within U1513E and U1513D
Depth (m CSF-A)
Unit I
Ooze
Pleistocene – Late Miocene
Unit II
Ooze/chalk and silicified limestone
Campanian – Cenomanian
Unit III
Claystone
Cenomanian
Unit IV
Claystone
Cenomanian – Albian
Unit V
Volcaniclastic-rich sandstone, with siltstone and silty claystone
early Aptian – Hauterivian
Unit VI
Basalt, dolerite, and volcaniclastic beds
Inclination
C34n
M1r
M3r
M5r
M6r
M8r
M9r
M10r
M10Nn.1n
Barremian
Hauterivian
Valanginian
121 Ma
126 Ma
130.5 Ma
<130.9 Ma
West
20.8m
East
U1513E
U1513D
Volcanic unit
D-66R-3, 93-105 Basalt
D-67R-2, 58-73 (Dyke)
D-69R-4, 76-95 Basalt
D-70R-4, 11-26 (Dyke)
D-71R-2, 110-124 Basalt
D-73R-4, 62-78 (Dyke)
D-74R-1, 120-132 (Dyke)
E-8R-4, 114-118 (Dyke)
weathering resistance
Basalt
Volcaniclastics
Intrusion
Flow boundaries
Sample (Petrography, XRF, XRD, $^{40}Ar/^{39}Ar$)

Figure 4:

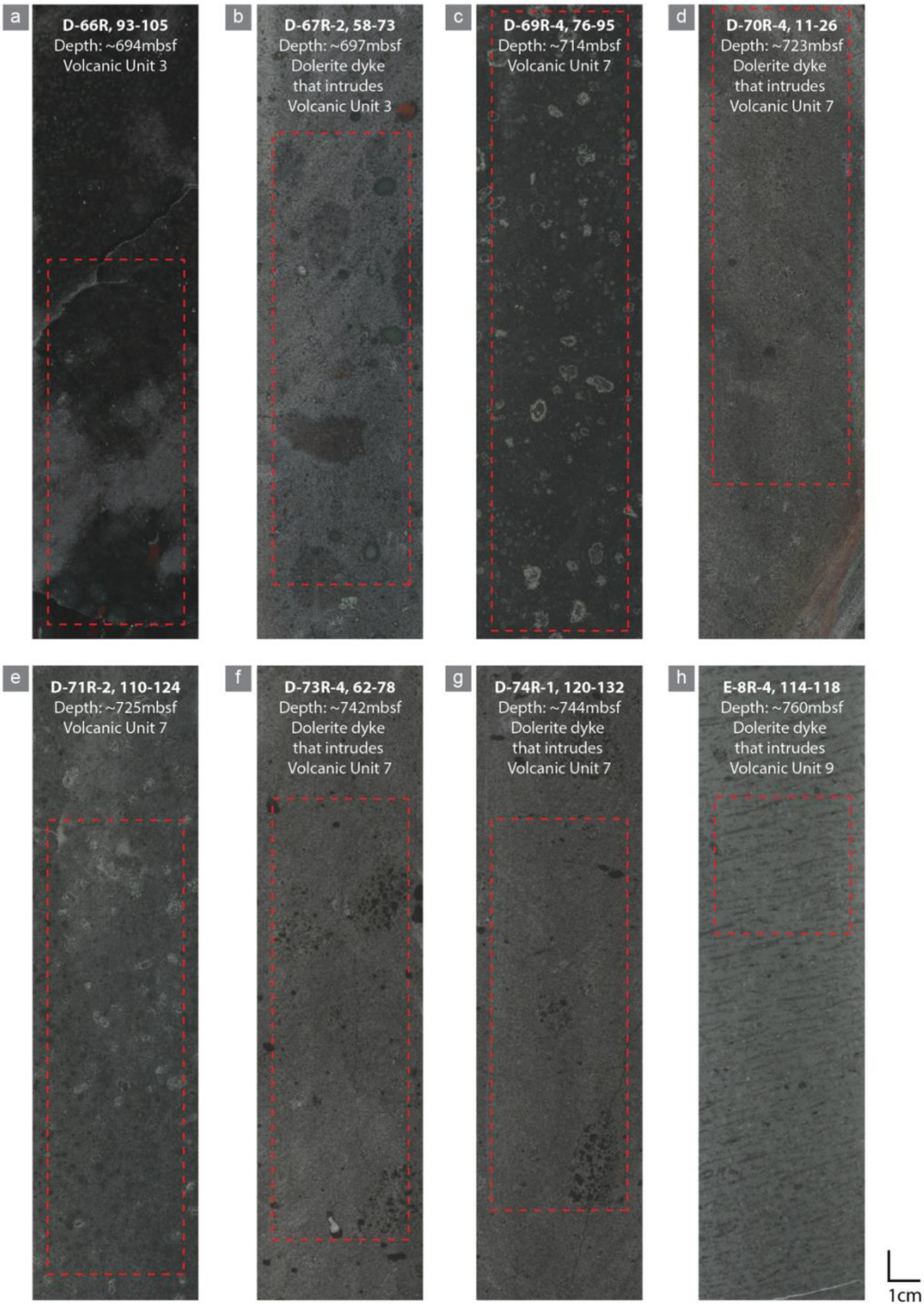

a
D-66R, 93-105
Depth: ~694mbsf
Volcanic Unit 3
b
D-67R-2, 58-73
Depth: ~697mbsf
Dolerite dyke
that intrudes
Volcanic Unit 3
c
D-69R-4, 76-95
Depth: ~714mbsf
Volcanic Unit 7
d
D-70R-4, 11-26
Depth: ~723mbsf
Dolerite dyke
that intrudes
Volcanic Unit 7
e
D-71R-2, 110-124
Depth: ~725mbsf
Volcanic Unit 7
f
D-73R-4, 62-78
Depth: ~742mbsf
Dolerite dyke
that intrudes
Volcanic Unit 7
g
D-74R-1, 120-132
Depth: ~744mbsf
Dolerite dyke
that intrudes
Volcanic Unit 7
h
E-8R-4, 114-118
Depth: ~760mbsf
Dolerite dyke
that intrudes
Volcanic Unit 9
1cm

Figure 5:

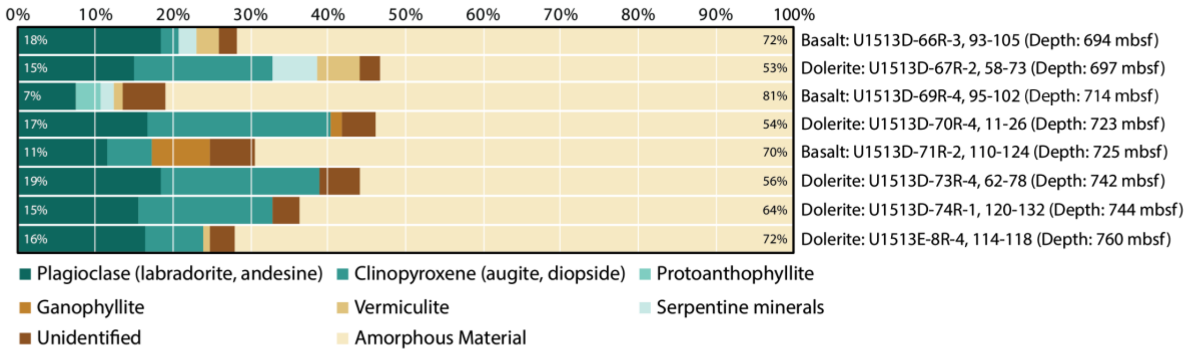
0%
10%
20%
30%
40%
50%
60%
70%
80%
90%
100%
18%
72%
Basalt: U1513D-66R-3, 93-105 (Depth: 694 mbsf)
15%
53%
Dolerite: U1513D-67R-2, 58-73 (Depth: 697 mbsf)
7%
81%
Basalt: U1513D-69R-4, 95-102 (Depth: 714 mbsf)
17%
54%
Dolerite: U1513D-70R-4, 11-26 (Depth: 723 mbsf)
11%
70%
Basalt: U1513D-71R-2, 110-124 (Depth: 725 mbsf)
19%
56%
Dolerite: U1513D-73R-4, 62-78 (Depth: 742 mbsf)
15%
64%
Dolerite: U1513D-74R-1, 120-132 (Depth: 744 mbsf)
16%
72%
Dolerite: U1513E-8R-4, 114-118 (Depth: 760 mbsf)
Plagioclase (labradorite, andesine)
Clinopyroxene (augite, diopside)
Protoanthophyllite
Ganophyllite
Vermiculite
Serpentine minerals
Unidentified
Amorphous Material

Figure 6:

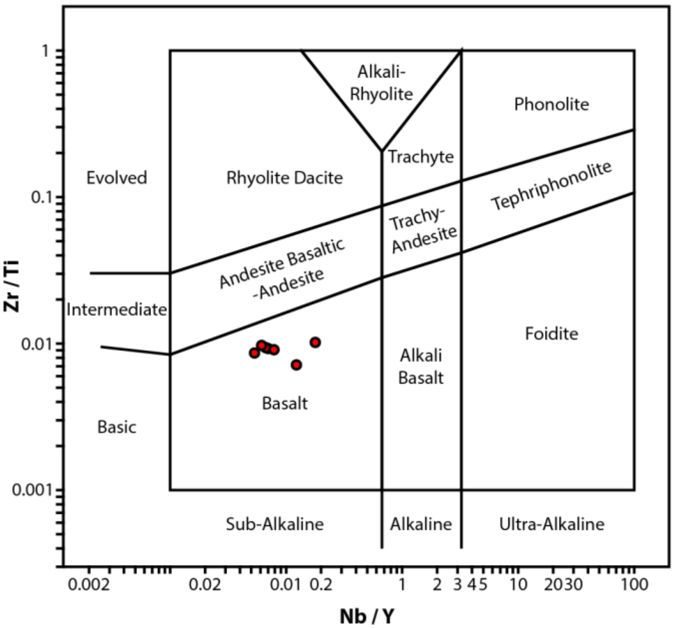
Alkali-
Rhyolite
Phonolite
Trachyte
Evolved
Rhyolite Dacite
Tephriphonolite
Trachy-
Andesite
Andesite Basaltic
-Andesite
Intermediate
Foidite
Alkali
Basalt
Basalt
Basic
Sub-Alkaline
Alkaline
Ultra-Alkaline
Zr / Ti
1
0.1
0.01
0.001
0.002
0.02
0.01
0.2
1
2
3
4
5
10
20
30
100
Nb / Y

Figure 7:

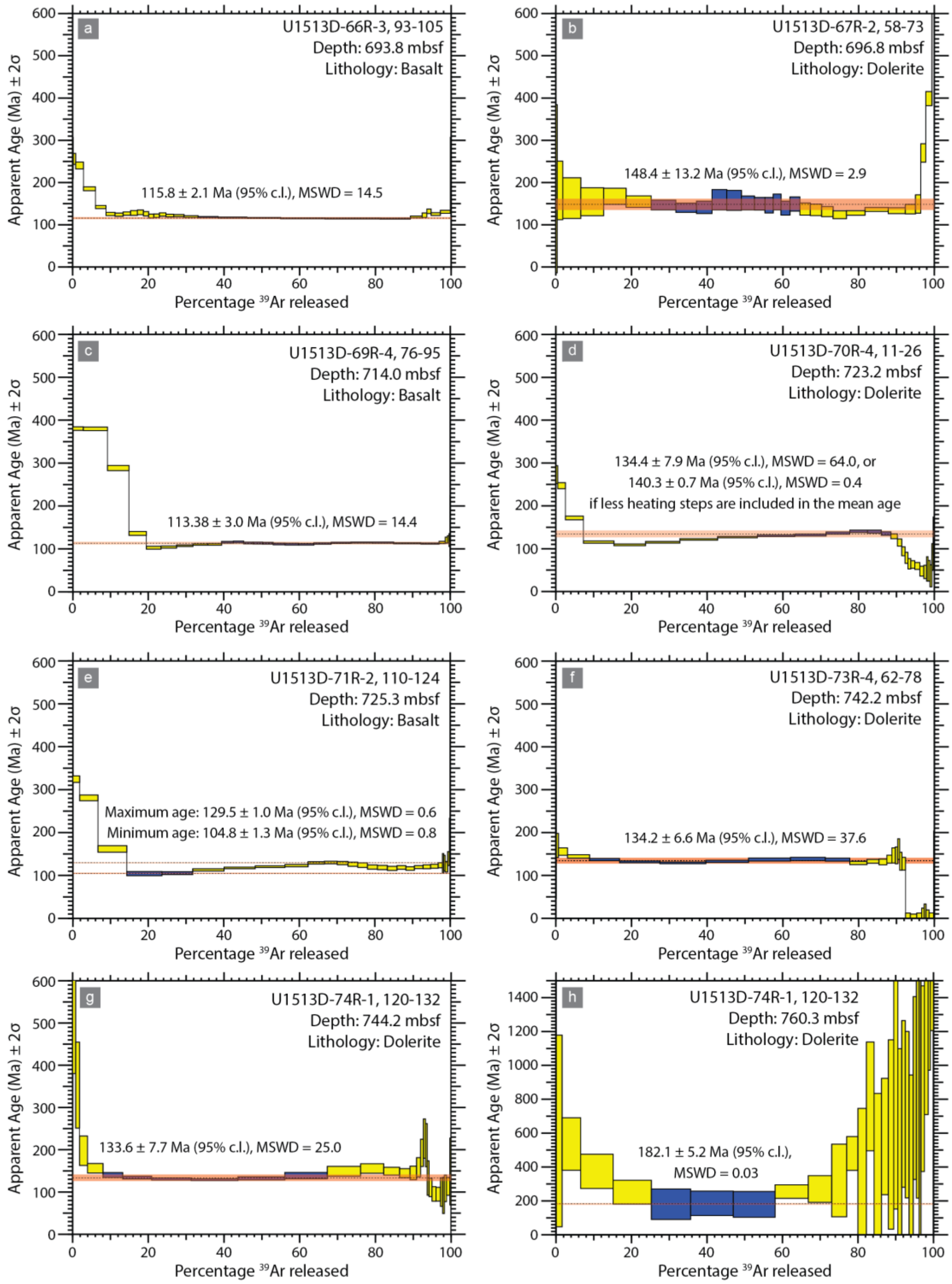
a
U1513D-66R-3, 93-105
Depth: 693.8 mbsf
Lithology: Basalt
115.8 ± 2.1 Ma (95% c.l.), MSWD = 14.5
b
U1513D-67R-2, 58-73
Depth: 696.8 mbsf
Lithology: Dolerite
148.4 ± 13.2 Ma (95% c.l.), MSWD = 2.9
c
U1513D-69R-4, 76-95
Depth: 714.0 mbsf
Lithology: Basalt
113.38 ± 3.0 Ma (95% c.l.), MSWD = 14.4
d
U1513D-70R-4, 11-26
Depth: 723.2 mbsf
Lithology: Dolerite
134.4 ± 7.9 Ma (95% c.l.), MSWD = 64.0, or
140.3 ± 0.7 Ma (95% c.l.), MSWD = 0.4
if less heating steps are included in the mean age
e
U1513D-71R-2, 110-124
Depth: 725.3 mbsf
Lithology: Basalt
Maximum age: 129.5 ± 1.0 Ma (95% c.l.), MSWD = 0.6
Minimum age: 104.8 ± 1.3 Ma (95% c.l.), MSWD = 0.8
f
U1513D-73R-4, 62-78
Depth: 742.2 mbsf
Lithology: Dolerite
134.2 ± 6.6 Ma (95% c.l.), MSWD = 37.6
g
U1513D-74R-1, 120-132
Depth: 744.2 mbsf
Lithology: Dolerite
133.6 ± 7.7 Ma (95% c.l.), MSWD = 25.0
h
U1513D-74R-1, 120-132
Depth: 760.3 mbsf
Lithology: Dolerite
182.1 ± 5.2 Ma (95% c.l.),
MSWD = 0.03
Apparent Age (Ma) ± 2σ
Percentage ³⁹Ar released

Figure 8:

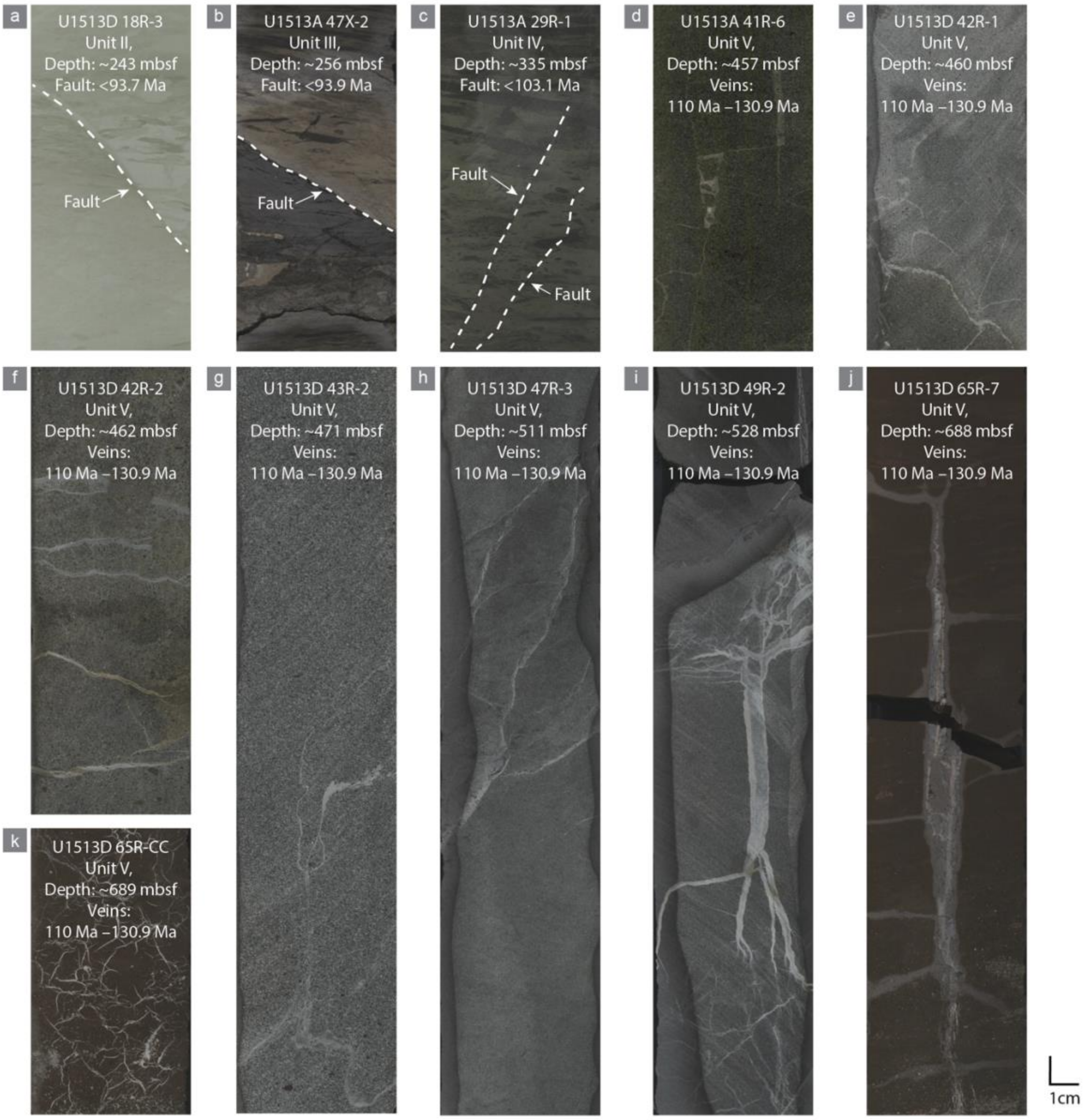
a
U1513D 18R-3
Unit II,
Depth: ~243 mbsf
Fault: <93.7 Ma
Fault
b
U1513A 47X-2
Unit III,
Depth: ~256 mbsf
Fault: <93.9 Ma
Fault
c
U1513A 29R-1
Unit IV,
Depth: ~335 mbsf
Fault: <103.1 Ma
Fault
Fault
d
U1513A 41R-6
Unit V,
Depth: ~457 mbsf
Veins:
110 Ma –130.9 Ma
e
U1513D 42R-1
Unit V,
Depth: ~460 mbsf
Veins:
110 Ma –130.9 Ma
f
U1513D 42R-2
Unit V,
Depth: ~462 mbsf
Veins:
110 Ma –130.9 Ma
g
U1513D 43R-2
Unit V,
Depth: ~471 mbsf
Veins:
110 Ma –130.9 Ma
h
U1513D 47R-3
Unit V,
Depth: ~511 mbsf
Veins:
110 Ma –130.9 Ma
i
U1513D 49R-2
Unit V,
Depth: ~528 mbsf
Veins:
110 Ma –130.9 Ma
j
U1513D 65R-7
Unit V,
Depth: ~688 mbsf
Veins:
110 Ma –130.9 Ma
k
U1513D 65R-CC
Unit V,
Depth: ~689 mbsf
Veins:
110 Ma –130.9 Ma
1cm

968 **Figure 9:**

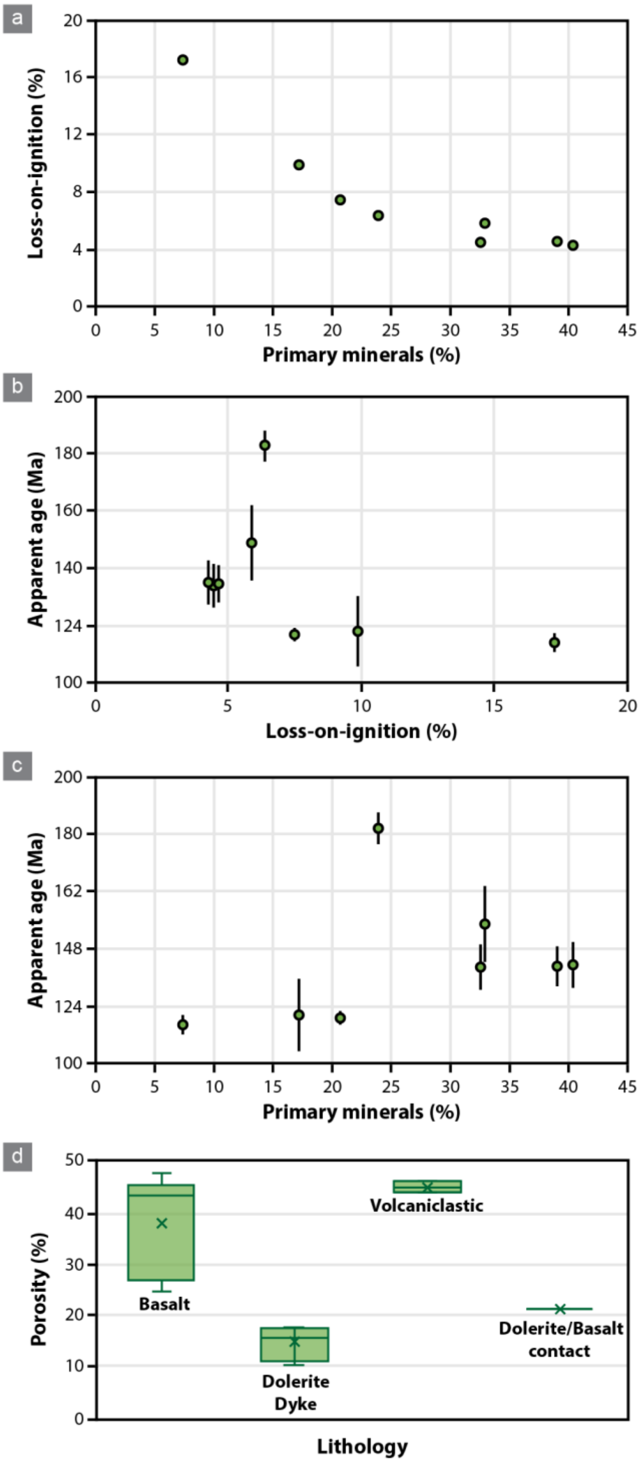

969

970

Figure 10:

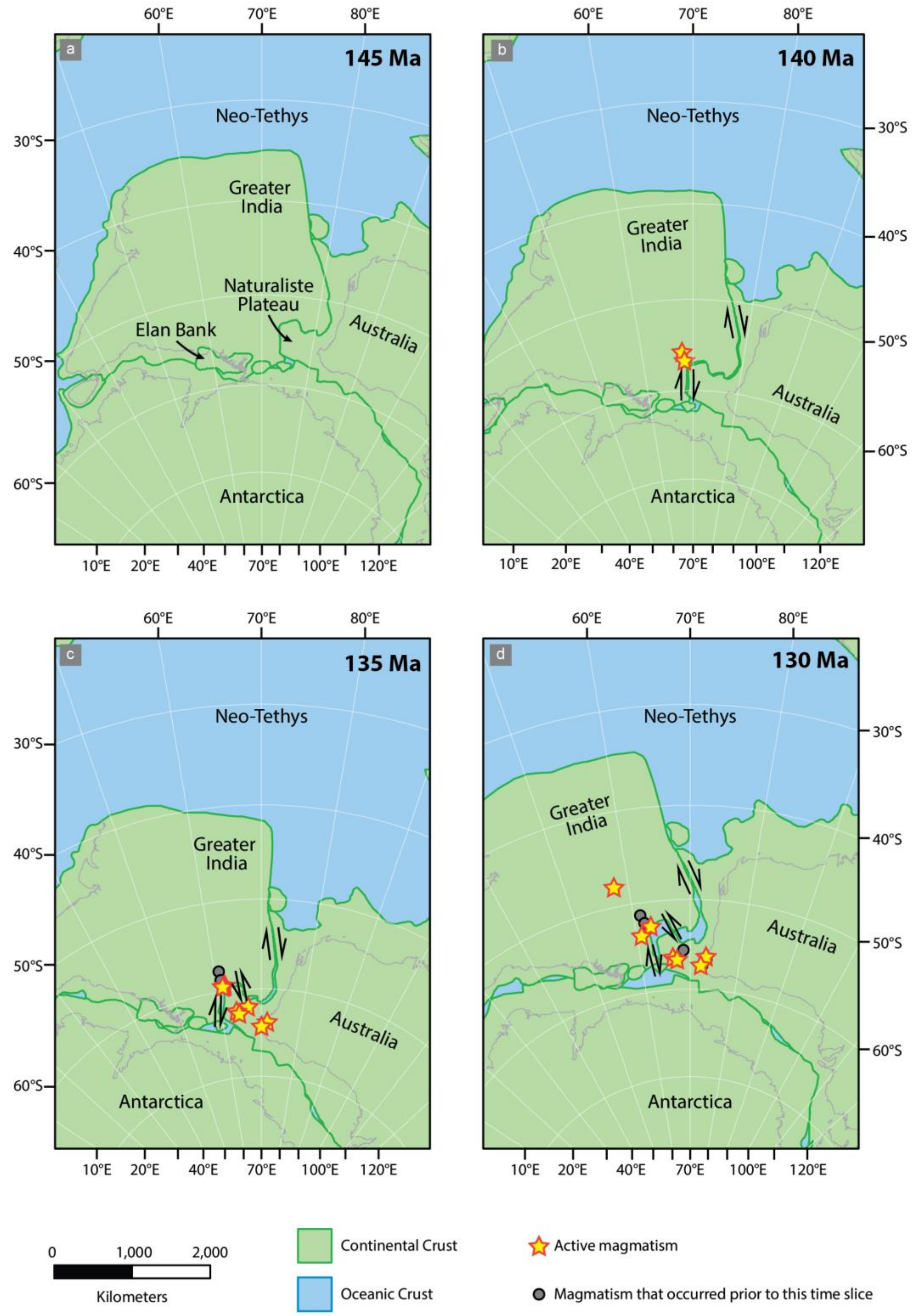
a
145 Ma
Neo-Tethys
Greater India
Naturaliste Plateau
Elan Bank
Australia
Antarctica
b
140 Ma
Neo-Tethys
Greater India
Australia
Antarctica
c
135 Ma
Neo-Tethys
Greater India
Australia
Antarctica
d
130 Ma
Neo-Tethys
Greater India
Australia
Antarctica
60°E
70°E
80°E
30°S
40°S
50°S
60°S
10°E
20°E
40°E
70°E
100°E
120°E
0
1,000
2,000
Kilometers
Continental Crust
Oceanic Crust
Active magmatism
Magmatism that occurred prior to this time slice

Figure 11:

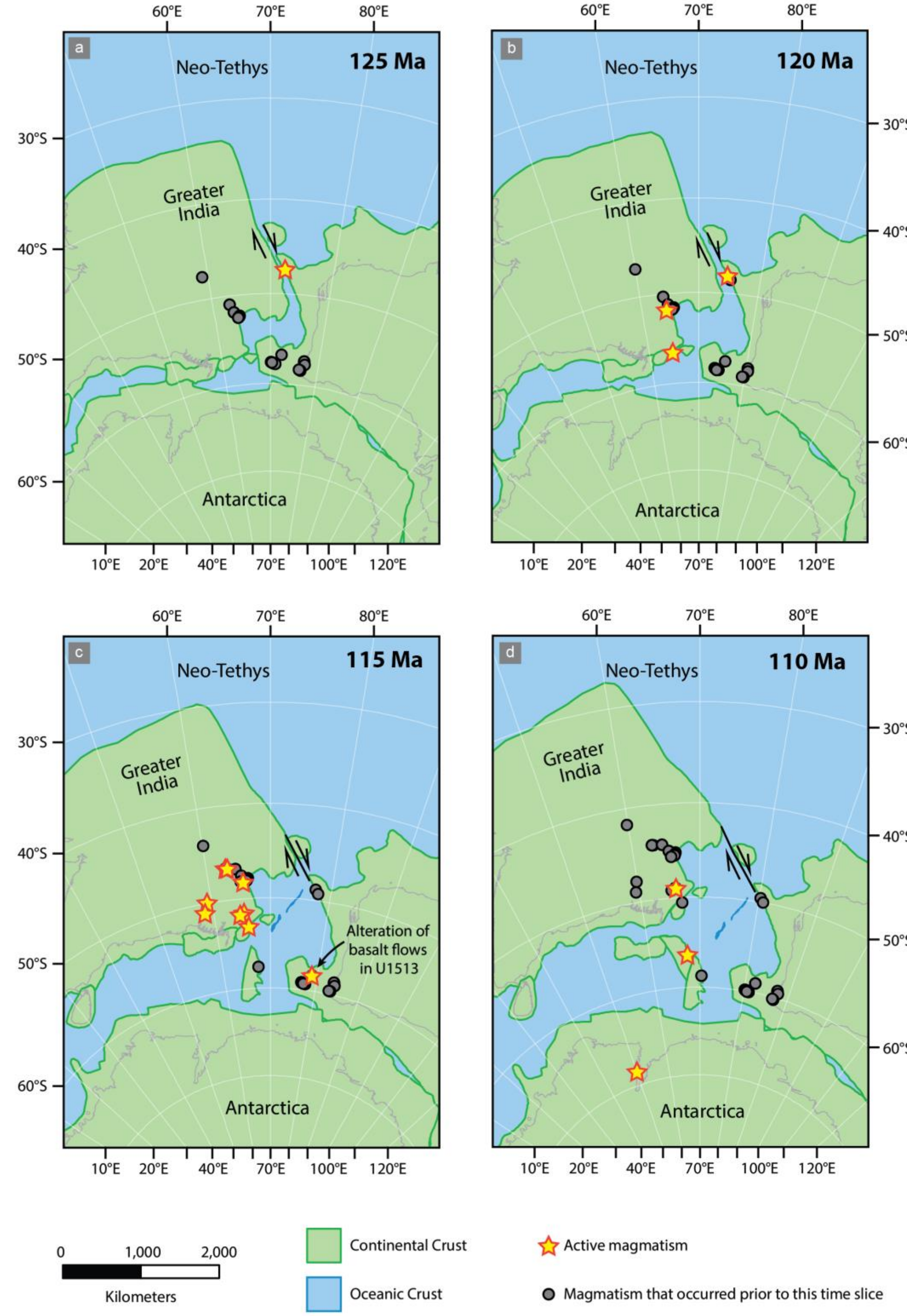
a
125 Ma
Neo-Tethys
Greater India
Antarctica
b
120 Ma
c
115 Ma
Alteration of basalt flows in U1513
d
110 Ma
60°E
70°E
80°E
30°S
40°S
50°S
60°S
10°E
20°E
40°E
70°E
100°E
120°E
0
1,000
2,000
Kilometers
Continental Crust
Oceanic Crust
Active magmatism
Magmatism that occurred prior to this time slice

Table 1: An overview of the details of each sample examined in this study, including the sample number, depth and metadata about the core number and section. Details about the lithologic units have been summarised from information provided in Tejada et al. (2020).

Lithologic Unit*	Lithology	IODP Sample Number	Hole	Core	Section	Top depth CSF-A (m)[1]	Bottom depth CSF-A (m)
Unit 3: A single, massive flow of high-MgO olivine-plagioclase-phyric basalt. It has a porphyritic texture, with large, bluish-white plagioclase phenocrysts within a microcrystalline groundmass. The basaltic flow is cross-cut by a dyke. The dyke has an equigranular texture as well as xenoliths of porphyritic basalt.	Basalt Flow	U1513D-66R-3, 93-105	D	66R	3-W	693.79	693.91
	Dolerite Dyke	U1513D-67R-2, 58-73	D	67R	2-W	696.78	696.93
Unit 7: Compound flows (thin- grading to several massive flows) of vesicular/amygdaloidal plagioclase- to olivine (altered)-pyroxene-phyric basalt. Some of the thin flows at the top of this unit are highly altered and have a trachytic texture. The flows grade downward to massive aphyric and sparsely vesicular/amygdaloidal massive flows at the base of the unit. Flow boundaries are marked by chilled margins or faults. The basaltic flows are cross-cut by multiple intrusions of steeply-dipping dykes with large plagioclase phenocrysts and xenoliths.	Basalt Flow	U1513D-69R-4, 76-95, U1513D-69R-4, 95-102	D	69R	4-W	713.96	714.22
	Dolerite Dyke	U1513D-70R-4, 11-26	D	70R	4-W	723.17	723.32
	Basalt Flow	U1513D-71R-2, 110-124, U1513D-71R-2, 124-130	D	71R	2-W	725.26	725.46
	Dolerite Dyke	U1513D-73R-4, 62-78	D	73R	4-W	742.23	742.39
	Dolerite Dyke	U1513D-74R-1, 120-132	D	74R	1-W	744.2	744.32
Unit 9: A compound flow of thin (cm-scale) flows of sparsely vesicular olivine-plagioclase-phyric basalt, grading downhole to massive flows of aphyric to olivine-pyroxene-plagioclase-phyric basalt. The basaltic flows are cross-cut by at least two dolerite dykes. The boundaries between the dyke and basalt flows are chilled margins or are faulted. The dykes also contain an apparent sub-horizontal planar fabric enhanced/caused by alteration along fractures.	Dolerite Dyke	U1513E-8R-4, 114-118, U1513E-8R-4, 118-119	E	8R	4-W	760.34	760.49

[1] CSF-A (m) refers to a specific International Ocean Discovery Program depth scale calculation. In this instance it is equivalent to meters below sea floor (mbsf) as has been used in the text.

Table 2. Major (wt %) and Trace (µg/g) element composition of samples from Site U1513 as determined by XRF. Loss-on-ignition (LOI) data are also included.

Hole	D	D	D	D	D	D	D	E
Core	66R	67R	69R	70R	71R	73R	74R	8R
Section	3-W	2-W	4-W	4-W	2-W	4-W	1-W	4-W
Top Depth (CSF-A m)[1]	693.79	696.78	714.15	723.17	725.26	742.23	744.20	760.34
Bottom Depth (CSF-A m)	693.91	696.93	714.22	723.32	725.40	742.39	744.32	760.38
SiO_2	44.81	45.75	42.56	47.59	44.84	48.32	48.38	44.91
TiO_2	0.38	0.52	1.01	1.15	1.04	1.11	1.15	1.91
Al_2O_3	22.11	18.29	15.39	15.09	16.66	14.63	14.24	18.36
Fe_2O_3T	5.33	7.55	9.90	11.90	10.01	10.38	10.88	10.54
MnO	0.10	0.15	0.14	0.20	0.16	0.24	0.24	0.43
MgO	7.86	9.66	7.95	6.49	7.68	7.17	7.13	6.85
CaO	9.57	9.70	3.00	10.43	6.67	10.63	10.56	6.61
Na_2O	2.08	2.22	1.91	2.48	2.64	2.63	2.51	3.44
K_2O	0.03	0.04	0.72	0.22	0.25	0.06	0.07	0.25
P_2O_5	0.04	0.04	0.01	0.10	0.08	0.10	0.11	0.20
LOI	7.43	5.83	17.29	4.22	9.85	4.53	4.40	6.32
Total	99.74	99.75	99.88	99.87	99.88	99.80	99.67	99.82
S	63	52	41	49	34	171	900	52
Cl	1199	768	3266	769	1736	480	624	17330
V	135	141	302	286	303	291	305	353
Cr	893	704	81	60	82	51	56	185
Co	59	48	43	42	47	49	41	78
Ni	325	320	54	30	41	43	48	97
Cu	58	53	58	29	39	68	69	98
Zn	46	59	95	76	87	78	81	131
Ga	11	12	14	16	17	16	15	25
Ge	< 0.5	< 0.5	1	2	1	< 0.5	2	< 0.5
Rb	1	1	13	7	5	1	1	3
Sr	155	124	168	157	178	159	158	215
Y	8	17	37	32	25	64	30	33
Zr	17	23	62	69	61	2	67	121
Nb	1	< 0.2	2	2	2	2	2	6
Cd	< 2.0	< 2.0	< 2.0	< 2.0	< 0.1	6	< 2.0	1
Sn	8	9	10	4	9	< 4.0	5	7
Cs	< 4.0	< 4.0	< 4.0	< 4.0	< 4.0	< 2.0	< 4.0	< 4.0
Ba	< 2.0	< 2.0	5	41	25	26	< 2.0	236
La	< 2.0	< 2.0	42	49	< 2.0	2	< 2.0	33
Hf	1	1	2	2	3	2	3	4
Pb	< 1.0	< 1.0	< 1.0	< 1.0	< 1.0	< 1.0	< 1.0	3
Th	< 1.0	< 1.0	< 1.0	< 1.0	< 1.0	< 1.0	< 1.0	< 1.0
U	< 1.0	< 1.0	< 1.0	< 1.0	< 1.0	< 1.0	< 1.0	< 1.0

[1] CSF-A (m) refers to a specific International Ocean Discovery Program depth scale calculation. In this instance it is equivalent to meters below sea floor (mbsf) as has been used in the text.

Table 3. Summary of $^{40}Ar/^{39}Ar$ whole-rock ages obtained from samples from basalt and dolerite samples from IODP Sites U1513D and U1513E. Please note that some of the samples yielded multiple potential ages. Further details about the argon dating methods and results are provided in Supplementary Files 4 and 5.

Sample	Mass (mg)	Total heating steps	Weighted Mean Age	Uncertainty (2σ)	MSWD[1]	Number of heating steps used in mean age	Proportion of ^{39}Ar released
U1513D-66R-3, 93-105 Basalt	135.4	29	115.8	2.1	14.5	6	55%
U1513D-67R-2, 58-73 Dolerite	122.9	29	148.4	13.2	2.9	11	38%
U1513D-69R-4, 76-95 Basalt	131.9	28	113.4	3.0	14.4	14	58%
U1513D-70R-4, 11-26 Dolerite	143.9	29	134.4	7.9	64.0	6	35%
			140.3	0.7	0.4	2	8%
U1513D-71R-2, 110-124 Basalt	132.8	29	104.8	1.3	0.8	2	17%
			129.5	1.0	0.6	3	11%
U1513D-73R-4, 62-78 Dolerite	137.7	29	134.2	6.6	37.6	7	68%
U1513D-74R-1, 120-132 Dolerite	130.9	29	133.6	7.7	25.0	6	58%
U1513E-8R-4, 118-119 Dolerite	121.2	28	182.1	5.2	0.03	3	32%

[1] Note that the high MSWD values reported here primarily reflects apparent age scatter associated with high precision results obtained for each heating step.

Table 4. Biostratigraphic and palaeomagnetic age control from Huber et al. (2019) from samples that were examined above and below sedimentary sequences that are cross-cut by faults and veins within material recovered from IODP Site U1513.

Hole-Core-Section	Fault/vein Depth Interval (CSF-A) m[1]	Veining	Biostratigraphic age control above faulted faulted/veined section (*)	Biostratigraphic age and palaeomagnetic age control below faulted/veined section (*, **)	Estimated timing of fault movement
U1513D-18R-3	242.67 m – 242.72 m	No	93.7 Ma (U1513D-16R-CC) B *Eprolithus moratus*	93.9 Ma (U1513D-20R-CC) T *Helena chiastia*	<93.7 Ma
U1513A-47X-2	256.44 – 256.48 m	No	93.9 Ma (U1513D-45X-3) T *Helena chiastia*	98.3 Ma (U1513D-47X-CC) B *Gartnerago segmentatum*	<93.9 Ma
U1513D-29R-1	335.09 – 335.21 m	No	103.1 Ma (U1513D-28R-CC) B *Eiffellithus turriseiffelii*	107.6 Ma (U1513D-31R-CC) B *Eiffellithus monechiae*	<103.1 Ma
U1513D-41R-6	457.03 – 458.13 m	Yes (calcite)	110.73 Ma (U1513-36R-CC) B *Tranolithus orionatus*	Base of M10Nn.1 (~130.9 Ma)***	110 Ma – 130.9 Ma
U1513D-42R-1	460.22 – 461.19 m	Yes (calcite)	110.73 Ma (U1513-36R-CC) B *Tranolithus orionatus*	Base of M10Nn.1 (~130.9 Ma)***	110 Ma – 130.9 Ma
U1513D-42R-2	461.22 – 462.60 m	Yes (calcite)	110.73 Ma (U1513-36R-CC) B *Tranolithus orionatus*	Base of M10Nn.1 (~130.9 Ma)***	110 Ma – 130.9 Ma
U1513D-43R-2	470.96 – 471.13 m	Yes (calcite)	110.73 Ma (U1513-36R-CC) B *Tranolithus orionatus*	Base of M10Nn.1 (~130.9 Ma)***	110 Ma – 130.9 Ma
U1513D-47R-3	511.41 – 511.83 m	Yes (calcite)	110.73 Ma (U1513-36R-CC) B *Tranolithus orionatus*	Base of M10Nn.1 (~130.9 Ma)***	110 Ma – 130.9 Ma
U1513D-49R-2	528.43 – 528.65 m	Yes (calcite)	110.73 Ma (U1513-36R-CC) B *Tranolithus orionatus*	Base of M10Nn.1 (~130.9 Ma)***	110 Ma – 130.9 Ma
U1513D-65R-7	688.04 – 688.97 m	Yes (calcite)	110.73 Ma (U1513-36R-CC) B *Tranolithus orionatus*	Base of M10Nn.1 (~130.9 Ma)***	110 Ma – 130.9 Ma

[1] CSF-A (m) refers to a specific International Ocean Discovery Program depth scale calculation. In this instance it is equivalent to meters below sea floor (mbsf) as has been used in the text.

U1513D-65R-CC	688.97–689.16 m	Yes (calcite)	110.73 Ma (U1513-36R-CC[2]) B *Tranolithus orionatus*	Base of M10Nn.1 (~130.9 Ma)	110 Ma – 130.9 Ma

*Sourced from Table T5 ‘Calcareous nannofossil bioevents, Site U1513’ of Huber et al. (2019)

**Sourced from Table T21 ‘Magnetic reversal depths and ages, Holes U1513B and U1513D’ of Huber et al. (2019)

***Numerical age proposed for the base of Unit V by Lee et al., (2020)

2 ‘CC’ refers to a sample that was collected from the Core Catcher at the base of the core section.